EUROPEAN ORGANISATION FOR NUCLEAR RESEARCH (CERN)

Submitted to: EPJC

CERN-EP-2022-133
10th November 2022

Constraints on spin-0 dark matter mediators and invisible Higgs decays using ATLAS 13 TeV pp collision data with two top quarks and missing transverse momentum in the final state

The ATLAS Collaboration

This paper presents a statistical combination of searches targeting final states with two top quarks and invisible particles, characterised by the presence of zero, one or two leptons, at least one jet originating from a b-quark and missing transverse momentum. The analyses are searches for phenomena beyond the Standard Model consistent with the direct production of dark matter in pp collisions at the LHC, using 139 fb^{-1} of data collected with the ATLAS detector at a centre-of-mass energy of 13 TeV. The results are interpreted in terms of simplified dark matter models with a spin-0 scalar or pseudoscalar mediator particle. In addition, the results are interpreted in terms of upper limits on the Higgs boson invisible branching ratio, where the Higgs boson is produced according to the Standard Model in association with a pair of top quarks. For scalar (pseudoscalar) dark matter models, with all couplings set to unity, the statistical combination extends the mass range excluded by the best of the individual channels by 50 (25) GeV, excluding mediator masses up to 370 GeV. In addition, the statistical combination improves the expected coupling exclusion reach by 14% (24%), assuming a scalar (pseudoscalar) mediator mass of 10 GeV. An upper limit on the Higgs boson invisible branching ratio of 0.38 ($0.30^{+0.13}_{-0.09}$) is observed (expected) at 95% confidence level.

Contents

1 Introduction

The existence of a non-luminous component of matter in the universe, dark matter (DM), is supported by compelling astrophysical evidence [1, 2]. The abundance of dark matter has been precisely determined from global fits of cosmological parameters to a variety of observations [3, 4]. Nevertheless, the nature of DM remains largely unknown.

In this paper, models where the DM candidate is a weakly interacting massive particle (WIMP) [5] are considered. In proton–proton (pp) collisions at the Large Hadron Collider (LHC), pair-produced WIMP DM does not interact with the detector and it can be detected only if produced in association with Standard Model (SM) particles, leading to signatures with missing transverse momentum. A wide range of experimental searches are focused on WIMP candidates at the LHC [6–12]. All recent searches are based on simplified benchmark models documented in the LPCC Dark Matter Working Group whitepapers [13–16]. Benchmark models are chosen to have a minimal number of additional parameters relative to the SM. This paper focuses on simplified models characterised by the introduction of a spin-0 particle mediator [15–23]. In this case, fermionic DM particle pairs are produced through the exchange of a colour-neutral scalar or pseudoscalar mediator (denoted by ϕ or a, respectively). In the Minimal Flavour Violation [24] assumption, the interaction between any new neutral spin-0 state and SM quarks is proportional to the fermion masses via Yukawa-type couplings and it is also treated as a free parameter of the model by means of a multiplicative factor g_q. Following Ref. [23], couplings to leptons and W/Z bosons, as well as explicit ϕ–H or a–H couplings of dimension four to the SM Higgs boson, are set to zero. The coupling of the mediator to the dark sector, g_χ, is not assumed to be proportional to the mass of the DM candidates and is treated simply as a free parameter.

The dominant production modes for such colour-neutral mediators are loop-induced gluon-fusion and associated production of the mediator with a top quark pair. Figures 1(a) and 1(b) show the two dominant production diagrams for the associated production of the mediator with a top quark pair. As discussed in Refs. [20, 25], the diagram in Figure 1(b) can be interpreted as the radiation of the mediator from a top quark. This process is enhanced for small energies and leads to a production cross section for scalar mediators about one order of magnitude larger than the one for pseudoscalar mediators for masses below the top quark threshold. The associated production of spin-0 mediators with a single top quark also has a sizeable, albeit non-dominant, cross section [19, 26, 27], especially for higher-mass mediators. The primary signal of interest in this paper is the associated production of a mediator particle with a pair of top quarks (DM+$t\bar{t}$), although sensitivity is also retained in the case of single top quark production (collectively referred to as DM+t). The relevant processes for DM+t are shown in Figures 1(c) and 1(d). The relative contribution of the two processes depends on the parameter space that is considered [26].

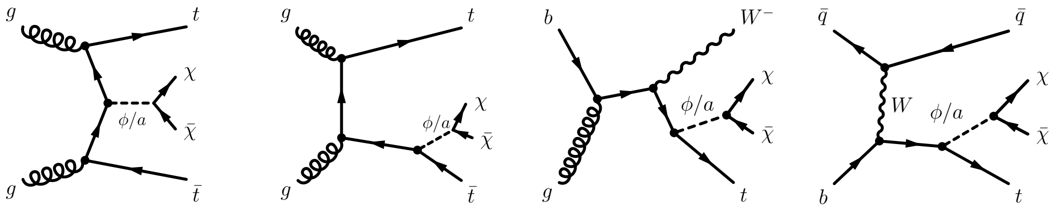

(a) (b) (c) (d)

Figure 1: Representative diagrams for spin-0 mediator associated production with (a) and (b) a top quark pair (DM+$t\bar{t}$), (c) a single top quark and a W boson (DM+tW) or (d) a single top quark and one (or more) jet(s) (DM+tj).

This paper presents a statistical combination of three searches targeting events with two top quarks and invisible particles, considering either zero- (tt0L [28]), one- (tt1L [29]) or two-lepton (tt2L [30]) final states, using 139 fb^{-1} of pp collisions data recorded by the ATLAS detector [31, 32] at a centre-of-mass energy of $\sqrt{s} = 13$ TeV. The tt0L analysis is extended and improved relative to that in Ref. [28], benefitting from the Run-2 improvements in the trigger selection of jets containing b-hadrons (b-jets) in ATLAS [33] that increase the sensitivity in models with low-mass mediators. The three analyses select independent (orthogonal) datasets which can be statistically combined to boost the sensitivity because they seek signal events in similar parts of the parameter space. Searches specifically targeting the associated production of a single top quark and invisible particles [34] are not orthogonal to the searches presented here. They are therefore not included and their combination is left as a future development.

The data are found to be in agreement with the SM background prediction in all selections considered in this paper. The statistical combination is used to set 95% confidence level (CL) constraints on the simplified DM models. The specific case where the mediator corresponds to the SM 125 GeV Higgs boson [35] is also considered when interpreting the results presented in this paper. It is referred to as the $H \rightarrow \text{inv}$ interpretation in the following. In the SM, the invisible Higgs boson branching ratio, $\mathcal{B}_{H\rightarrow\text{inv}}$, is 0.12% from $H \rightarrow ZZ \rightarrow 4\nu$ decays [36], and higher branching ratios to invisible particles are predicted by Higgs–dark-matter portal models [37–50]. Results on the invisible branching ratio obtained from the statistical combination of previous ATLAS searches conducted with the Run-1 and partial Run-2 dataset reported an observed (expected) limit of 0.26 (0.17) [51], while CMS reported 0.19 (0.15) [52] at 95% CL. Recent updates by the ATLAS and CMS Collaborations in the vector-boson-fusion channel report improved observed (expected) upper limits of 0.145 (0.103) [53] and 0.18 (0.10) [54], respectively, using the full Run-2 dataset.

The paper is structured as follows. The experimental dataset and the simulated event samples are presented in Section 2, the new and previously published searches are introduced in Section 3, and their statistical combination, including the treatment of correlated systematic uncertainties is discussed in Section 4. Results in terms of exclusion limits are presented in Section 5, followed by the conclusions in Section 6. Finally, additional details of the extended 0-lepton channel analysis are discussed in Appendix A.

2 Data and simulated event samples

The dataset used in the analyses described in this paper consists of pp collision data recorded by the ATLAS detector [31, 32] at a centre-of-mass energy of $\sqrt{s} = 13$ TeV with stable beam conditions. The ATLAS detector is a multipurpose particle detector with a forward–backward symmetric cylindrical geometry and nearly full coverage in solid angle.[1] It consists of an inner tracking detector surrounded by a thin superconducting solenoid providing a 2 T axial magnetic field, electromagnetic and hadron calorimeters, and a muon spectrometer. An extensive software suite [55] is used in data simulation, in the reconstruction and analysis of real and simulated data, in detector operations, and in the trigger and data acquisition systems of the experiment.

All collision events considered in this paper are required to have at least one reconstructed interaction vertex with a minimum of two associated tracks, each having $p_{\mathrm{T}} > 500$ MeV. In events with multiple vertices, the one with the highest sum of squared transverse momenta of associated tracks is chosen as the primary vertex [56]. Electrons [57], muons [58], τ-leptons [59] and jets are reconstructed by combining the signals from the different components of the ATLAS detector. Small-radius jets are reconstructed from energy deposits in the calorimeters using the anti-k_t jet algorithm [60, 61] with a radius parameter of $R = 0.4$. Reclustered large-radius jets [62, 63] are reconstructed with the same algorithm, using a radius parameter of $R = 1.2$ and with small-radius jets as input, unless otherwise specified. Multivariate algorithms are used to identify small-R jets with $p_{\mathrm{T}} > 20$ GeV containing b-hadrons (b-jets) [64, 65]. This is referred to as b-tagging. The missing transverse momentum $\boldsymbol{p}_{\mathrm{T}}^{\mathrm{miss}}$ (with magnitude $E_{\mathrm{T}}^{\mathrm{miss}}$) is calculated from the negative vector sum of the transverse momenta of electrons, muons and jet candidates, and an additional 'soft term' [66] which includes tracks found in the tracking system that originate from the primary vertex but are not associated with any reconstructed object.

Depending on the analysis channel, events are selected by lepton triggers [67, 68], $E_{\mathrm{T}}^{\mathrm{miss}}$ triggers [69] or b-jet triggers [33]. The uncertainty in the combined integrated luminosity is 1.7% [70], obtained using the LUCID-2 detector [71] for the primary luminosity measurements. Events accepted by lepton and $E_{\mathrm{T}}^{\mathrm{miss}}$ triggers are required to meet the standard ATLAS data-quality assessment criteria [72] to ensure that all subdetector systems were functioning normally. This leads to an integrated luminosity of 3.2 fb^{-1}, 33.0 fb^{-1}, 44.3 fb^{-1} and 58.5 fb^{-1} in 2015, 2016, 2017 and 2018 data-taking, respectively, with a total integrated luminosity of 139.0 fb^{-1}. Events accepted by b-jet triggers are required to meet additional criteria ensuring that the online beam-spot position measurement is valid, which leads to the exclusion

---

[1] ATLAS uses a right-handed coordinate system with its origin at the nominal interaction point (IP) in the centre of the detector and the z-axis along the beam pipe. The x-axis points from the IP to the centre of the LHC ring, and the y-axis points upward. Cylindrical coordinates (r, ϕ) are used in the transverse plane, ϕ being the azimuthal angle around the z-axis. The pseudorapidity is defined in terms of the polar angle θ as $\eta = -\ln\tan(\theta/2)$. The angular distance between two objects in η–ϕ space is defined by $\Delta R \equiv \sqrt{(\Delta\eta)^2 + (\Delta\phi)^2}$.

of the 2015 data and to a reduced integrated luminosity of 24.6 fb^{-1}, 43.7 fb^{-1} and 57.7 fb^{-1} in 2016, 2017 and 2018 data-taking, respectively, with a total integrated luminosity of 126.0 fb^{-1}. The b-jet trigger chains considered in this paper require at least four jets, among which two jets are b-tagged by the online version of the b-tagging boosted decision tree algorithm [65].

Dedicated Monte Carlo (MC) simulated event samples are used to aid in the estimation of the background from SM processes and to model the dark matter or invisible Higgs boson signal. All simulated events were processed through a simulation of the ATLAS detector and its response [73, 74]. The simulated events are reconstructed with the same algorithms as used for data. They contain a realistic modelling of additional pp collisions in the same or neighbouring bunch crossings (pile-up), obtained by overlaying minimum-bias events simulated using the soft QCD processes of Pythia 8.186 [75, 76] with the NNPDF2.3lo set of parton distribution functions (PDFs) [77] and the A3 [78] set of tuned parameters.

Standard Model processes producing one or two top quarks were modelled using Powheg Box v2 [79–82] and normalised to cross sections calculated to next-to-next-to-leading-order (NNLO) plus next-to-next-to-leading-logarithm (NNLL) [83] accuracy in QCD. Processes involving the production of one (two) vector boson(s) were simulated using Sherpa 2.2.1 (2.2.2) [84–88] and normalised to cross sections at NNLO [89] (NLO) accuracy in QCD. The $t\bar{t}{+}V$ ($V = W, Z$), tZ and tWZ processes were modelled by MadGraph5_aMC@NLO 2.3.3 [90] and normalised to NLO cross-section accuracy in QCD [36, 90]. Lastly, $t\bar{t}H$ background events, with visible Higgs boson decay modes, were generated by Powheg Box v2.

Signal samples for dark matter produced in association with a $t\bar{t}$ pair (DM+$t\bar{t}$) were generated using a leading-order (LO) matrix element, with up to one extra parton, in the MadGraph5_aMC@NLO 2.6.7 [90] generator interfaced to Pythia 8.244 and using the CKKW-L merging algorithm [91]. The five-flavour scheme NNPDF3.0nlo [92] PDF set was used. The top quark decay was simulated using MadSpin [93]. Signal cross sections for this process were calculated to NLO QCD accuracy using the same version of MadGraph, as suggested in Ref. [25]. Models with a DM particle mass of 1 GeV and $g_q = g_\chi = 1$ are considered, while the masses of the mediators range from 10 GeV to 400 GeV. The typical scaling factors from LO to NLO in these calculations range between 1.25 and 1.35, depending on the mediator mass and whether it is a scalar or a pseudoscalar boson. Signal samples for dark matter produced in association with a single top quark were generated using the same settings as for the DM+$t\bar{t}$ samples. For these signal models, the tW and the tj processes were generated separately. Each one was normalised to the LO cross section predicted by the model and then the samples were combined. No extra partons were generated from the matrix element in this case.

Signal samples modelling Higgs boson production in association with a $t\bar{t}$ pair ($t\bar{t}H$) were generated using the Powheg Box v2 [94] generator at NLO with the NNPDF3.0nlo [92] PDF set. The tWH signal samples were produced with MadGraph5_aMC@NLO 2.6.2 in the five-flavour scheme with the NNPDF3.0nnlo PDF set. The top quark and W boson decays were handled by MadSpin to account for spin correlations among the decay products. The overlap of the tWH process with $t\bar{t}H$ at NLO was removed by using a diagram removal technique [95, 96]. Contributions arising from tH production in the t-channel and s-channel are below 0.1% and are therefore neglected. In these samples, the Higgs boson decays via ZZ^* into neutrinos, and events are normalised using the total cross section at NLO QCD and electroweak accuracy recommended by the LHC Higgs Cross Section Working Group [36, 96, 97].

For the SM background samples, except those generated using Sherpa, the EvtGen 1.2.0 [98] program was used to simulate the properties of the b- and c-hadron decays, and Pythia 8.186 with the A14 tune [99] was used for the parton showering, hadronisation model and underlying event. For the Sherpa generator, the default Sherpa [84–88] configuration recommended by its authors was used.

The modelling of the response of the various ATLAS subdetectors was performed using Geant4 [74] for all the background MC samples, while all signal MC samples were simulated using a faster simulation based on a parameterisation of the calorimeter response and Geant4 for the other detector systems [73].

3 Experimental signatures and analysis strategy

Each of the analyses requires the presence of at least one b-tagged jet and $E_{\mathrm{T}}^{\mathrm{miss}}$ in the event. To further suppress events where the $E_{\mathrm{T}}^{\mathrm{miss}}$ originates from mismeasurements, the ratio of the $E_{\mathrm{T}}^{\mathrm{miss}}$ to its resolution is used to construct the event's missing transverse momentum significance [100], $\mathcal{S}$.

The tt0L analysis targets decay chains with no leptons in the final state. The tt0L analysis published in Ref. [28] focuses on a set of signal regions (SR), referred to as tt0L-high in this paper, defined so as to obtain maximal significance for the targeted signal events. It uses the $E_{\mathrm{T}}^{\mathrm{miss}}$ triggers to select events with large missing transverse momentum and requires at least one highly energetic, hadronically decaying top quark candidate. An additional set of SRs, referred to as tt0L-low, is presented for the first time in this paper and extends the previously published results by relying on a combination of $E_{\mathrm{T}}^{\mathrm{miss}}$ and b-tagged jet triggers to retain events with lower-momentum jets that fail one of the tt0L-high analysis criteria.

The two other analyses considered in this paper target leptonic final states. The tt1L analysis [29] selects events with exactly one lepton (e or μ) and it is based on the $E_{\mathrm{T}}^{\mathrm{miss}}$ triggers. The tt2L analysis [30] targets events with exactly two opposite-charge leptons (e or μ) in the final states selected with dilepton triggers.

Common event-quality criteria and object reconstruction and identification definitions for leptons, jets, b-tagged jets and $E_{\mathrm{T}}^{\mathrm{miss}}$ are applied in all analyses considered in the combination. Minimum p_{T} requirements of 4.5 GeV and 20 GeV are applied to leptons and jets, respectively. The lepton multiplicity requirements guarantee that the 0-lepton, 1-lepton and 2-lepton channels are by construction non-overlapping. Further kinematics, isolation and identification requirements are applied to each object in the individual analysis channels and optimised for each topology. These details, together with the details of the reconstruction algorithms, quality requirements and efficiencies can be found in Refs. [28–30] and in Appendix A.1. For all analyses in this paper, background-enriched selections (control regions, CR) are defined so as to allow the data to aid in the estimation of the dominant SM backgrounds, and validation regions (VR) are used to verify the robustness of these estimates. A dedicated background estimation strategy was developed for each channel [28–30], using independent control regions for all dominant SM processes.

Observed and expected event yields in the signal and control regions are used in Poisson probability functions to build likelihood functions, which are combined in a profile likelihood fit. A profile likelihood ratio is employed in the $\mathrm{CL_s}$ method to exclude at 95% CL the signal-plus-background hypothesis for the signal models considered [101–104].

3.1 Description of analysis channels

The tt0L analysis The experimental signature targeted in this channel consists of at least four jets, two of which are b-tagged, and large missing transverse momentum ($E_{\mathrm{T}}^{\mathrm{miss}} > 160$ GeV). Events with electrons, muons or τ-leptons are rejected. The tt0L-high selection consists of events with high missing transverse momentum ($E_{\mathrm{T}}^{\mathrm{miss}}$ trigger, $E_{\mathrm{T}}^{\mathrm{miss}} > 250$ GeV, $\mathcal{S} > 14$) where at least one of the reconstructed large-radius jets ($R = 1.2$) has a mass consistent with one produced from a boosted hadronic top quark decay. This selection corresponds to signal region selections SRA and SRB in Ref. [28], which were originally optimised to be sensitive to high-mass supersymmetric partners of the top quark and are divided into three categories (TT, TW and T0), depending on whether the subleading large-radius jet ($R = 1.2$) has an invariant mass consistent with a top quark, a W boson or neither. Given the signature and kinematic similarity between the signal considered in this paper and top squark pairs decaying into a top quark and a neutralino, these regions can also be used to constrain DM+$t\bar{t}$ models. SRA and SRB are orthogonal because of a requirement on the χ^2-based stransverse mass variable, m_{T2,χ^2}, and are statistically combined. This stransverse mass [105, 106] variable is designed to reconstruct the mass of two heavy particles produced in an event and decaying symmetrically into an invisible particle and a top quark, as expected in supersymmetric top quark topologies. It relies on a χ^2-based method to identify the hadronically decaying top quark candidates. The background estimation in SRA and SRB is aided by means of dedicated control regions for all dominant SM processes: $t\bar{t}Z$, Z+jets, $t\bar{t}$, single top quark in the tW channel, and W+jets. Event yields with updated jet calibrations [107] were recalculated with respect to Ref. [28] and are presented in Figure 2(a). The yield change due to the new calibration is between 6% and 15% and is reflected in the signal predictions as well. This is because the new calibration decreases the contribution of events with artificially increased missing transverse momentum, due to mismeasured jets in the analysis, by reducing the tails of the missing transverse momentum significance distribution. This translates to a slightly higher signal-to-background ratio in the tt0L-high SRs.

The tt0L-low selection is newly added in this paper with the aim of improving the sensitivity of the 0-lepton channel for dark matter models by selecting final states with lower missing transverse momentum and/or lower-momentum objects. The tt0L-low selection is therefore designed to maximise the sensitivity to DM+$t\bar{t}$ signals with low mediator masses ($m(\phi), m(a) < 100$ GeV). Events are selected by a combination of $E_{\mathrm{T}}^{\mathrm{miss}}$ triggers and b-jet triggers. Events selected with $E_{\mathrm{T}}^{\mathrm{miss}}$ triggers must fulfil $E_{\mathrm{T}}^{\mathrm{miss}} > 250$ GeV to ensure the triggers are fully efficient. In addition, they are required to have either $\mathcal{S} < 14$ or no large-radius jets consistent with highly energetic top quark candidates to ensure orthogonality with the tt0L-high selections. Events selected with b-jet triggers must fulfil the requirement that the missing transverse momentum be between 160 and 250 GeV. The lower bound suppresses the multi-jet background contamination, while the upper bound ensures orthogonality with tt0L-high. The online b-tagged jet candidates must match the offline b-tagged jet candidates within a cone of $\Delta R = 0.2$.

Three signal regions are defined, SR0X, SRWX and SRTX, according to the mass of the heaviest large-radius jet, which is used to infer the p_{T} of the most energetic top quark in the event. SR0X requires that no large-radius jets (0) are present, while in SRWX and SRTX the mass of the heaviest large-radius jet has to be respectively lower or higher than 130 GeV, i.e. in the neighbourhood of the W boson (W) or top quark (T) mass.

An optimal categorisation of the events in which a top quark is produced is particularly important in the tt0L-low analysis because of the high top quark background rate and its large variation with respect to the top quark transverse momentum. In order to maximise the correlation of the large-radius jet mass with the p_{T} of the most energetic top quark, jet reconstruction in the tt0L-low analysis uses a smaller radius parameter value ($R = 1.0$) than in the tt0L-high analysis. This is associated with newly introduced lower selections on the large-radius jet transverse momentum ($p_{\mathrm{T}} > 200$ GeV), and invariant mass ($m_{\text{large-radius jet}} > 40$ GeV). A requirement rejecting high-mass, large-radius jets with radius parameter $R = 1.2$, as defined in the tt0L-high analysis, is also applied to ensure orthogonality between the two analyses.

The final states targeted in the tt0L-low analysis are less energetic than in the tt0L-high analysis, such that the decay products of the top quarks are expected to be less collimated. Hence no subleading large-radius jet is required (X).

The full list of requirements for the three tt0L-low signal regions is reported in Table 1. Three angular separation variables are used: $\Delta\phi_{\mathrm{min}}(\boldsymbol{p}_{\mathrm{T},1\text{-}4}, \boldsymbol{p}_{\mathrm{T}}^{\mathrm{miss}})$ to reduce the contamination from multi-jet events, $\Delta R\left(b_1, b_2\right)$ to reduce the contamination from b-jets from gluon splitting as present in Z+jets events, and ΔR_{min}(large-radius jet, b-tagged jets) to enhance the fraction of events with hadronic top quark decays, as in the signal. The SM background originating from the top quark is reduced by using the $\cosh_{\mathrm{max}}$ variable. This variable aims to identify events where a leptonically decaying W boson is the source of all $E_{\mathrm{T}}^{\mathrm{miss}}$ in the event because the lepton is not reconstructed. The hyperbolic cosine of the pseudorapidity difference between the missed W boson candidate and each of the two b-tagged jets selected in the event is estimated, and the $\cosh_{\mathrm{max}}$ variable is defined to be the larger of the two values:

$$\cosh_{\mathrm{max}} = \max\{\cosh\Delta\eta^{1}_{W,b}, \cosh\Delta\eta^{2}_{W,b}\}.$$

The value of $\cosh\Delta\eta_{W,b}$ is estimated by solving the kinematics of the top quark decay, assuming $m_W \ll p_{\mathrm{T}}^{W} \cdot \cosh\eta_W \sim E_{\mathrm{T}}^{\mathrm{miss}} \cdot \cosh\eta_W$, given that $E_{\mathrm{T}}^{\mathrm{miss}} > 160$ GeV and $\cosh\eta_W \geq 1$. For events with $t\bar{t}$ pairs decaying fully hadronically, the approximation $p_{\mathrm{T}}^{W} \sim E_{\mathrm{T}}^{\mathrm{miss}}$ is not valid, resulting in unphysical values, e.g. $\cosh_{\mathrm{max}} < 1$, while events with high $\cosh_{\mathrm{max}}$ values are likely to contain a top quark decaying leptonically and are excluded from the signal regions. Since the signal events have two hadronically decaying top quarks, while most of the backgrounds have one or none, a χ^2-based variable, $\chi^2_{t\bar{t},\,\mathrm{had}}$, is used to identify events with a hadronically decaying top quark pair (Appendix A.1). The $\chi^2_{t\bar{t},\,\mathrm{had}}$ variable is constructed using up to six jets in the event and using the b-tagging classification when appropriate to reconstruct the two W bosons and the two top quarks in the event. Invariant mass constraint terms for these particles are used to build the χ^2. All possible jet assignments are tested and the one with the lowest χ^2 is chosen. The event distributions for the $\cosh_{\mathrm{max}}$ and the $\chi^2_{t\bar{t},\,\mathrm{had}}$ variables are each shown in Figure 3 after applying all the SR0X selection requirements except those on the variable presented in the distribution. The transverse momentum of the $t\bar{t}$ system ($p_{\mathrm{T}}^{t\bar{t}}$) constructed with the $\chi^2_{t\bar{t},\,\mathrm{had}}$ method is compared with the $E_{\mathrm{T}}^{\mathrm{miss}}$. In signal events these two quantities are expected to have similar values, so events with $p_{\mathrm{T}}^{t\bar{t}}/E_{\mathrm{T}}^{\mathrm{miss}}$ values outside a window containing unity are excluded.

Table 1: Selection criteria for the signal regions used in the tt0L-low analysis.

Variables	**SR0X**	**SRWX**	**SRTX**
N_{lepton}	$= 0$		
Orthogonalisation	$E_{\mathrm{T}}^{\mathrm{miss}} < 250$ GeV or $\mathcal{S} < 14$ or $m^{R=1.2}_{\text{large-radius jet}} < 120$ GeV		
$E_{\mathrm{T}}^{\mathrm{miss}}$ [GeV]	> 160 < 250, when passing b-jet triggers		
$\mathcal{S}$	> 10		
$\Delta\phi_{\mathrm{min}}(\boldsymbol{p}_{\mathrm{T},1\text{-}4}, \boldsymbol{p}_{\mathrm{T}}^{\mathrm{miss}})$	> 1.0	> 0.5	
$\Delta R\left(b_1, b_2\right)$	> 1.2		
$N_{\text{large-radius jet}}$	$= 0$	> 0	
$m_{\text{large-radius jet}}$ [GeV]	—	(40, 130)	≥ 130
ΔR_{min}(large-radius jet, b-tagged jets)	—		< 1.2
$\cosh_{\mathrm{max}}$	< 0.5	< 0.6	< 0.7
$\chi^2_{t\bar{t},\,\mathrm{had}}$	< 4	< 6	< 8
$p_{\mathrm{T}}^{t\bar{t}}/E_{\mathrm{T}}^{\mathrm{miss}}$	(0.7, 1.2)	(0.5, 1.2)	

The main contribution to the SM background in the signal regions originates from single-top-quark events in the tW channel and $t\bar{t}$ events, with a lepton missed by the reconstruction algorithms, and $Z \rightarrow \nu\nu$ events

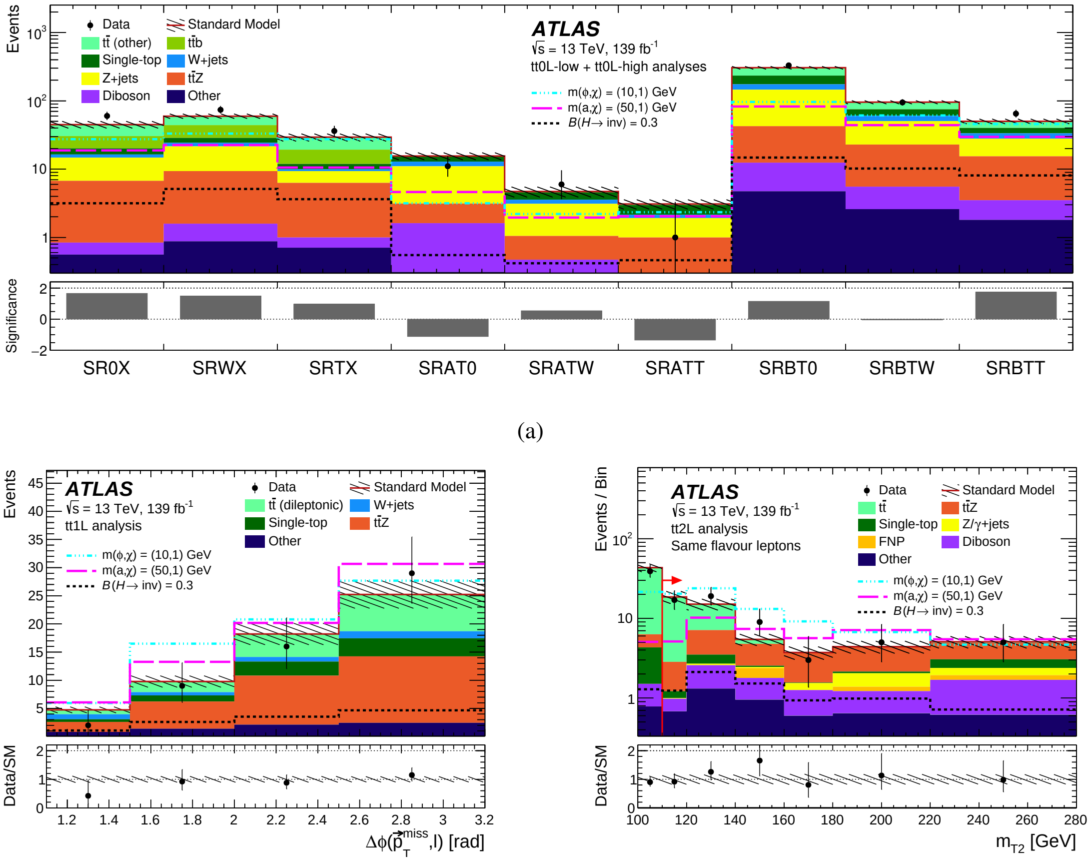

(a)

(b)

(c)

Figure 2: (a) Post-fit signal region yields for the tt0L-high and the tt0L-low analyses. The bottom panel shows the statistical significance [108] of the difference between the SM prediction and the observed data in each region. The definitions of SRAT0, SRATW, SRATT, SRBT0, SRBTW and SRBTT can be found in Ref. [28]. Representative post-fit distributions are presented for (b) the tt1L and (c) the tt2L analyses: each bin of these distributions, starting from the red arrow in (c), corresponds to a single SR included in the fit. In the tt0L-low analysis, '$t\bar{t}$ (other)' represents $t\bar{t}$ events without extra jets or events with extra light-flavour jets. In the tt2L analysis, 'FNP' includes the contribution from fake/non-prompt lepton background arising from jets (mainly π/K, heavy-flavour hadron decays and photon conversion) misidentified as leptons, estimated in a purely data-driven way. 'Other' includes contributions from $t\bar{t}$+W, tZ and tWZ processes, and also $t\bar{t}$ (semileptonic) for the tt1L analysis. The total uncertainty in the SM expectation is represented with hatched bands and the expected distributions for selected signal models are shown as dashed lines.

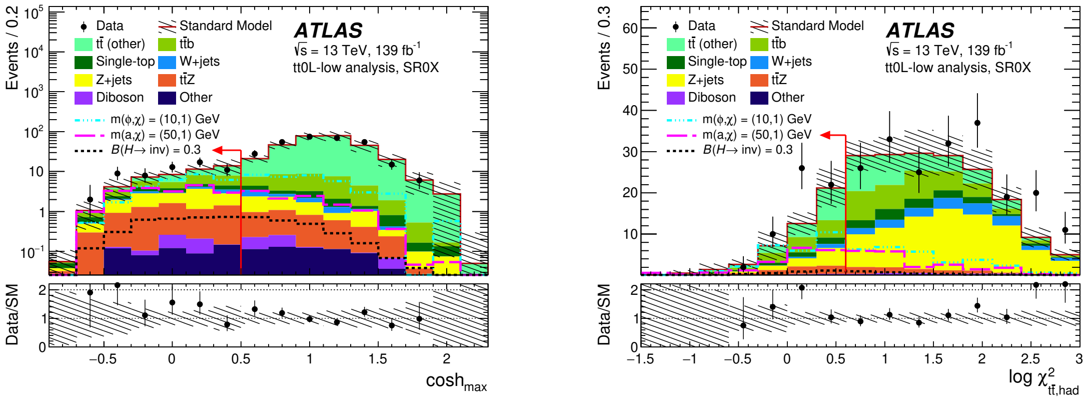

(a)

(b)

Figure 3: Distributions of (a) $\cosh_{\mathrm{max}}$ and (b) $\chi^2_{t\bar{t},\,\mathrm{had}}$ in SR0X events passing all the SR requirements except those on the variable being presented (which are indicated by the arrows). The contributions from all SM backgrounds are shown after the simultaneous profile likelihood fit to all tt0L-low CRs, with the hatched bands representing the total uncertainty. The category '$t\bar{t}$ (other)' represents $t\bar{t}$ events without extra jets or events with extra light-flavour jets. 'Other' includes contributions from $t\bar{t}$+W, tZ and tWZ processes. The expected distributions for selected signal models are shown as dashed lines. The underflow (overflow) events are included in the first (last) bin. The bottom panels show the ratio of the observed data to the total SM background prediction, with the hatched area representing the total uncertainty in the background prediction.

(Z+jets, $t\bar{t}$+Z). Unlike in the tt0L-high SRs, $t\bar{t}$ is the dominant contribution in the tt0L-low selections, due to the lower $E_{\mathrm{T}}^{\mathrm{miss}}$ requirements. Dedicated control regions are used to aid the background estimation in the signal regions for all dominant processes. These CRs are similar to the ones in the tt0L-high analysis for single top quarks in the tW channel, Z+jets and $t\bar{t}$+Z. No control regions are defined for W+jets since it represents less than 5% of the total background in all three tt0L-low signal regions. Due to the importance of the $t\bar{t}$ background in the tt0L-low selections, $t\bar{t}$ events with extra b-hadrons ($t\bar{t}$+b) are treated separately from $t\bar{t}$ events without extra jets or events with extra light-flavour jets (referred to as *other*) in the tt0L-low analysis, and distinct control regions are defined for each of the two components. This is done because $t\bar{t}$+b events are more likely to pass the signal region selections than $t\bar{t}$ (other) events because of the presence of extra b-jets, which makes it more difficult to isolate and reconstruct the $t\bar{t}$ system. In practice, the $t\bar{t}$ (other) and $t\bar{t}$+b event distributions exhibit a significant shape difference in the $\cosh_{\mathrm{max}}$ variable. Moreover, the observed simulation mismodelling for $t\bar{t}$+b events is larger than for $t\bar{t}$ (other) events and can be corrected for by separating the two components.

The background estimates are validated in dedicated, non-overlapping, validation regions, which require zero leptons and are orthogonal to the signal region selections. In these regions, the background prediction agrees with the data to within one standard deviation (1σ). More details are given in Appendix A.2.

The expected numbers of events are estimated in a simultaneous profile likelihood fit to all tt0L-low CRs, and are shown in Table 2. The observed data are compatible with the prediction, agreeing to within 2σ in each signal region.

The results presented in this paper show the final combination of the tt0L-low and tt0L-high analyses. The details of this combination and the single-channel individual limits are discussed in Appendix A.3.

Table 2: Expected and observed numbers of events in SR0X, SRWX and SRTX. The background yields and uncertainties are shown after the simultaneous profile likelihood fit to all tt0L-low CRs. The category '$t\bar{t}$ (other)' represents $t\bar{t}$ events without extra jets or events with extra light-flavour jets. 'Other' includes contributions from $t\bar{t}$+W, tZ and tWZ processes. The quoted background uncertainties include both the statistical and systematic contributions, while the signal uncertainties are purely statistical.

Process	**SR0X**	**SRWX**	**SRTX**
Observed data	60	74	36
Expected SM events	45 ± 8	59 ± 6	28 ± 5
$t\bar{t}$ (other)	14 ± 4	15 ± 4	9.4 ± 3.5
$t\bar{t}$+b	10 ± 7	15.0 ± 3.1	7.2 ± 2.8
Single-top	3.8 ± 3.0	4.3 ± 2.6	1.9 ± 1.5
Z+jets	8.0 ± 1.6	12.1 ± 2.3	3.1 ± 0.8
W+jets	1.6 ± 1.1	2.7 ± 2.1	0.6 ± 0.6
$t\bar{t}$+Z	5.9 ± 1.0	7.8 ± 1.3	5.3 ± 1.1
Diboson	0.28 ± 0.20	0.7 ± 0.4	0.30 ± 0.19
Other	0.55 ± 0.15	0.88 ± 0.24	0.70 ± 0.22
Pre-fit $t\bar{t}$	15	17	9.8
Pre-fit $t\bar{t}$+b	7	11.5	5.6
Pre-fit Single-top	7.1	8.2	3.6
Pre-fit Z+jets	6.1	9.2	2.3
Pre-fit $t\bar{t}$+Z	5.9	7.9	5.4
Benchmark signal models			
DM $m(\phi, \chi)$ = (10, 1) GeV	27.4 ± 2.4	33.2 ± 2.2	27.5 ± 2.2
DM $m(a, \chi)$ = (50, 1) GeV	18.8 ± 1.3	22.6 ± 1.5	10.6 ± 1.0
$H \rightarrow$ inv ($\mathcal{B}$ = 100%)	10.52 ± 0.34	17.1 ± 0.4	12.1 ± 0.4

The tt1L analysis This analysis requires exactly one lepton (e or μ), at least four jets, two of which must be b-tagged, and $E_{\mathrm{T}}^{\mathrm{miss}} > 230$ GeV, and was designed to target spin-0 DM models. The $E_{\mathrm{T}}^{\mathrm{miss}}$ significance $\mathcal{S}$ must be above 15 and, only for this analysis, it considers only jets and leptons in the events and their resolution, as described in Ref. [109]. A recursive variable-radius reclustering algorithm [110] is applied to the jets to identify at least one large-variable-radius jet loosely consistent with a top quark ($m_{\mathrm{top}^{\mathrm{reclustered}}} > 150$ GeV). The use of a variable-radius algorithm, instead of a fixed-radius one, increases the acceptance of both highly boosted events and less boosted events when no explicit categorisation is performed. In addition, a requirement on the 'topness' likelihood variable [111] is used to distinguish between the signal and dileptonic decays in SM $t\bar{t}$ events where one of the leptons is misidentified or outside the acceptance. This variable quantifies how well each event satisfies the dileptonic $t\bar{t}$ hypothesis, using the top quark and W boson mass constraints and a requirement that the centre-of-mass energy of the event is minimised. The $E_{\mathrm{T}}^{\mathrm{miss}}$ triggers were used to select data that then populate this SR. This region is divided into four disjoint regions according to the azimuthal distance between the $E_{\mathrm{T}}^{\mathrm{miss}}$ and the lepton momentum, $\Delta\phi(\boldsymbol{p}_{\mathrm{T}}^{\mathrm{miss}}, \ell)$, which is presented in Figure 2(b) and is found to be larger for pseudoscalar mediator models. The binning also maximises the sensitivity for scalar mediator models, which are more similar to the background but are characterised by a larger production cross section at low masses. An additional requirement of $\Delta\phi(\boldsymbol{p}_{\mathrm{T}}^{\mathrm{miss}}, \ell) > 1.1$ is applied to suppress the SM background. The dominant backgrounds, $t\bar{t}$ and $t\bar{t}Z$, are estimated by means of dedicated CRs.

The tt2L analysis The last analysis considers events with two opposite-charge leptons (e or μ), at least one b-tagged jet and large values of $E_{\mathrm{T}}^{\mathrm{miss}}$ significance ($\mathcal{S} > 12$), exploiting events collected with dilepton triggers. Events are then separated into two categories depending on whether the two leptons have the same or different flavour, and in the same-flavour selection an additional requirement of $|m_{\ell\ell} - m_Z| > 20$ GeV is added to suppress the Z+jets background. In this selection, the main discriminating variable is the leptonic stransverse mass m_{T2} [105, 106], which is used to bound the individual masses of a pair of identical particles that are each presumed to have decayed into one visible and one invisible particle. This quantitiy is used to bound dileptonic top pair decays. To maximise the search sensitivity, the m_{T2} spectrum is divided into six bins, starting from 110 GeV. The m_{T2} distribution for selected events with two leptons with the same flavour is presented in Figure 2(c). In this search, the main backgrounds are from $t\bar{t}$, $t\bar{t}Z$, single-top-quark tW-channel, Z+jets, and diboson processes. These backgrounds are estimated with MC simulations and normalised with data in orthogonal CRs for the dominant contributions ($t\bar{t}$ and $t\bar{t}Z$), while the background arising from fake/non-prompt leptons is estimated directly from the data.

3.2 Orthogonalisation

In order to combine the results of the different searches, the searches are required to be statistically independent and any possible overlaps of kinematic regions were investigated and removed as described in the following. The three analysis channels are disjoint because of their requirements on lepton multiplicity. The tt0L-high and tt0L-low channels are kept orthogonal by the requirements on the large-radius jet as well as on the $E_{\mathrm{T}}^{\mathrm{miss}}$ and its significance, $\mathcal{S}$. In addition, one of the Z+jets CRs in the tt0L-high analysis, denoted by CRZAB-T0 in Ref. [28], is not considered and a single control region, CRZAB-TTTW, is used to normalise the Z+jets process in all SRs of the tt0L-high analysis. This has negligible impact on the tt0L-high analysis results and it is done to ensure orthogonality between the Z+jets CRs in the tt0L-high and tt0L-low analyses, as those events are used to normalise the Z+jets background in the tt0L-low analysis. To the same end, the Z+jets CR in the tt0L-low analysis only selects events with either $N_{\text{large-radius jet}} < 2$ or subleading large-radius jet mass < 60 GeV.

The CRs used to normalise the $t\bar{t}Z$ background overlap. The three analysis channels share a common strategy to determine the amount of $t\bar{t}Z$ (with $Z \to \nu\nu$) background in their SRs. The strategy is to construct CRs requiring three charged leptons in order to maximise their $t\bar{t}Z$ (with $Z \to \ell\ell$) event content, which once determined can be scaled by the ratio of $Z \to \nu\nu$ to $Z \to \ell\ell$ branching fractions. These control regions differ only in minor selections adapted to the SR of each specific channel. In the combination, the $t\bar{t}Z$ estimation is harmonised by using the most inclusive $\mathrm{CR}_{t\bar{t}Z}$, from the tt2L analysis [30], as a common CR across all channels. The fitted normalisation parameter value obtained in the combination is consistent within 1% with the one published in Ref. [29].

4 Statistical combination and uncertainties

The statistical combination of the analyses considered in this paper consists of maximising a profile likelihood ratio [102] constructed from the product of the individual analysis likelihoods:

$$\Lambda(\alpha;\theta) = \frac{L\left(\alpha, \hat{\hat{\theta}}(\alpha)\right)}{L\left(\hat{\alpha}, \hat{\theta}\right)}.$$

The α and θ parameters represent, respectively, the parameter of interest and the nuisance parameters. In the numerator, the nuisance parameters are set to their profiled values $\hat{\hat{\theta}}(\alpha)$, which maximise the likelihood function for fixed values of the parameter of interest α. In the denominator, both the parameter of interest and the nuisance parameters are set to the values that jointly maximise the likelihood: $\hat{\alpha}$ and $\hat{\theta}$, respectively.

For the DM signal model interpretations, upper limits on the signal cross section are calculated following the CL_s formalism, using the profile likelihood ratio as a test statistic. The parameter of interest is the overall signal strength, defined as a scale factor multiplying the cross section predicted by the signal hypothesis, and it is bounded from below by zero. The final result is provided as a ratio of the lowest excluded signal cross section to the predicted cross section with all couplings set to unity. For the $H \rightarrow \text{inv}$ signal model interpretation, the branching fraction $\mathcal{B}_{H\rightarrow\text{inv}}$ is considered as the parameter of interest α, following the implementation described in Refs. [112, 113].

As described in Section 3, for each channel the estimation of the dominant SM backgrounds is aided by means of dedicated control regions that constrain free-floating normalisation factors for each of these backgrounds.

Systematic uncertainties are modelled in the likelihood function as nuisance parameters θ constrained by Gaussian or log-normal probability density functions [114].

Three types of sources of systematic uncertainty are considered: detector-related (experimental) uncertainties, uncertainties related to the modelling of SM background processes, and uncertainties related to the modelling of the signal processes. Regarding the experimental and SM modelling uncertainties, all details are given in Refs. [28–30] respectively for the zero-, one- and two-lepton channels. The tt0L-low channel includes the same uncertainties as the tt0L-high channel and, in addition, uncertainties associated with the b-jet trigger efficiencies. The typical size of these uncertainties is a few percent. All analyses use common event-quality criteria and object reconstruction and identification definitions. For this reason, all experimental systematic uncertainties are treated as correlated across channels in the statistical combination. The dominant sources of experimental systematic uncertainty in the combination are the uncertainties related to the jet energy scale and resolution, followed by either flavour-tagging uncertainties or uncertainties related to the missing transverse momentum, depending on the analysis channel.

Uncertainties in the modelling of the SM background processes in MC simulation and their theoretical cross-section uncertainties are also taken into account. All modelling uncertainties are treated as uncorrelated across different channels as they probe different regions of the available phase space.

Uncertainties related to the MC modelling of the DM signals include fragmentation and renormalisation scale uncertainties, and the uncertainties related to the modelling of the parton shower. The impact of these uncertainties varies from 10% to 25%. Uncertainties related to the $t\bar{t}H$ with $H \rightarrow \text{inv}$ signal modelling also include fragmentation and renormalisation scale uncertainties, parton shower uncertainties and PDF uncertainties. Among these, scale uncertainty effects, which are evaluated in the simplified template cross-section formalism [36, 115], are the dominant contribution and range between 7% and 17%. Signal modelling uncertainties are treated as fully correlated across analysis channels.

All sources of uncertainty in the SM backgrounds are summarised in Figure 4. In most of the SRs, the dominant systematic uncertainties are the ones related to theory predictions and MC modelling, while jet uncertainties are the dominant experimental ones. No significant difference from either the composition or the value of the total uncertainty presented in the published individual analyses is observed.

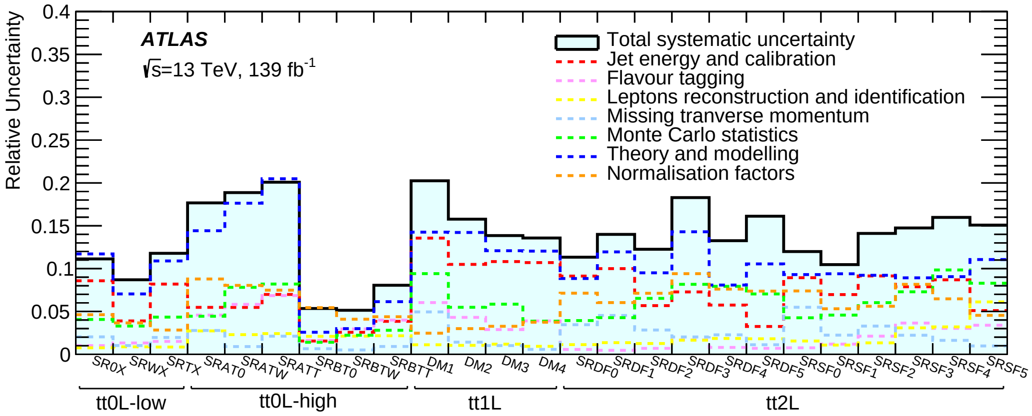

Figure 4: Summary of the total uncertainty in the background prediction for each SR of the tt0L-low, tt0L-high, tt1L, and tt2L analysis channels in the statistical combination. Their dominant contributions are indicated by individual lines. Individual uncertainties can be correlated, and do not necessarily add up in quadrature to the total background uncertainty.

5 Exclusion limits

Exclusion limits at 95% CL are presented in Figures 5(a) and 5(b) for DM models with a spin-0 scalar or pseudoscalar mediator particle, respectively. The three individual channels are also presented for comparison. The tt0L limits are the result of the statistical combination of the tt0L-low and tt0L-high SRs. The tt0L-low selection improves the expected scalar (pseudoscalar) mediator stand-alone cross-section limit of the tt0L-high by up to 15% (5%) and it is strongest for mediator masses values around 10 GeV. Details of the comparison can be found in Appendix A.3.

The signal generation considered in these results includes both the top-quark-pair final states (DM+$t\bar{t}$) and single-top-quark final states (DM+tW and DM+tj). The limits are expressed in terms of the ratio of the excluded cross section to the nominal cross section for a coupling of $g = g_q = g_\chi = 1$. With these assumptions, scalar DM models are characterised by a higher cross section than for pseudoscalar DM models with low mediator masses [20], while the two models have very similar cross sections beyond the top quark decay threshold ($m(\phi)$ or $m(a) \sim 2 \cdot m_t$). A DM particle mass of 1 GeV is considered, although the results are valid as long as the mass of the mediator is larger than twice the mass of the DM particle. The solid (dashed) lines show the observed (expected) exclusion limits for each individual analysis and their statistical combination. For scalar (pseudoscalar) DM models, the combination extends the excluded mass range by 50 (25) GeV beyond that of the best of the individual analyses, excluding mediator masses up to 370 GeV. In addition, the combination improves the expected cross-section limits by 14% and 24%, for low-mass scalar and pseudoscalar DM mediators, respectively. This directly translates into more stringent exclusion limits on the couplings. When only the associated production of DM and two top quarks is considered in the interpretation of the results, the excluded scalar (pseudoscalar) mediator mass range obtained from the combination is reduced by 70 (20) GeV relative to the sensitivity of the combination as reported in Figures 5(a) and 5(b). As the production of DM in association with a single top quark is most relevant for higher masses in the scalar mediator models [26], the impact of this process for masses below 50 GeV is negligible. In contrast, for the pseudoscalar mediator models, the ratio of single-top-quark channel to $t\bar{t}$ channel cross sections is relatively constant [26]. When considering only DM+$t\bar{t}$ associated production, the cross-section upper limit weakens by about 18% over the whole mass range.

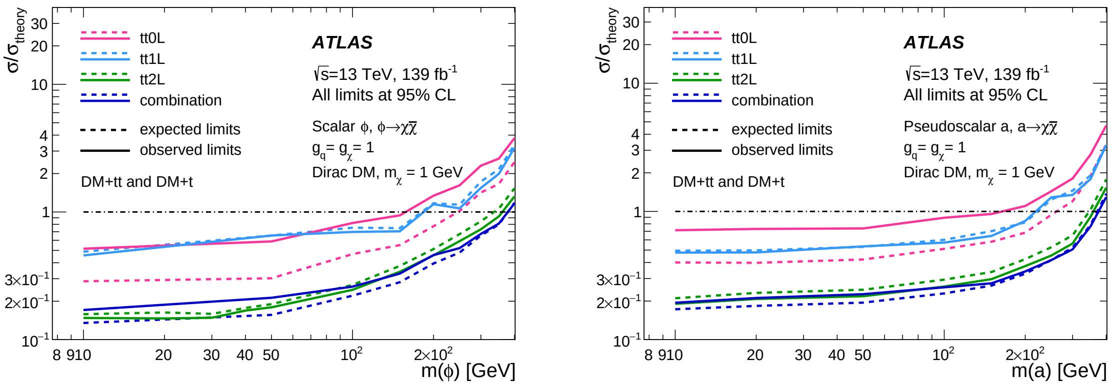

(a)

(b)

Figure 5: Exclusion limits for colour-neutral (a) scalar or (b) pseudoscalar mediator dark matter models as a function of the mediator mass $m(\phi)$ or $m(a)$ for a DM mass $m_\chi = 1$ GeV. Associated production of DM with both single top quarks (tW and tj channels) and top quark pairs is considered. The limits are calculated at 95% CL and are expressed in terms of the ratio of the excluded cross section to the cross section for a coupling assumption of $g = g_q = g_\chi = 1$. The solid (dashed) lines show the observed (expected) exclusion limits for each individual channel and their statistical combination.

The negative logarithmic profile likelihood ratios $-2\,\Delta\ln(\Lambda)(\mathcal{B}_{H\to\mathrm{inv}};\theta)$ as a function of $\mathcal{B}_{H\to\mathrm{inv}}$ from the individual analyses and their combination are shown in Figure 6.

Expected results are obtained using the Asimov dataset technique and calculated from asymptotic formulae [102]. The best-fit values of $\mathcal{B}_{H\to\mathrm{inv}}$ for the individual analyses are compatible, agreeing to within one standard deviation. Their statistical combination yields a best-fit value of $0.08^{+0.15}_{-0.15}$, consistent with the SM prediction of 0.12%. The combined observed 95% CL upper limit on $\mathcal{B}_{H\to\mathrm{inv}}$ is 0.38 while the expected value is $0.30^{+0.13}_{-0.09}$. The individual analysis results are presented in Table 3, while the details of the tt0L combination are reported in Appendix A.3. The overall uncertainty is dominated by the statistical uncertainty of the data and, to a lesser extent, by systematic uncertainties associated with the modelling of the SM processes and jet-related uncertainties. Higgs boson invisible decays represent a specific case of the DM simplified models considered in the previous section, where the mass of the scalar mediator is assumed to be 125 GeV. The two results are compatible with each other, when taking into account the different order of accuracy used in event generation for the $H \to \mathrm{inv}$ model.

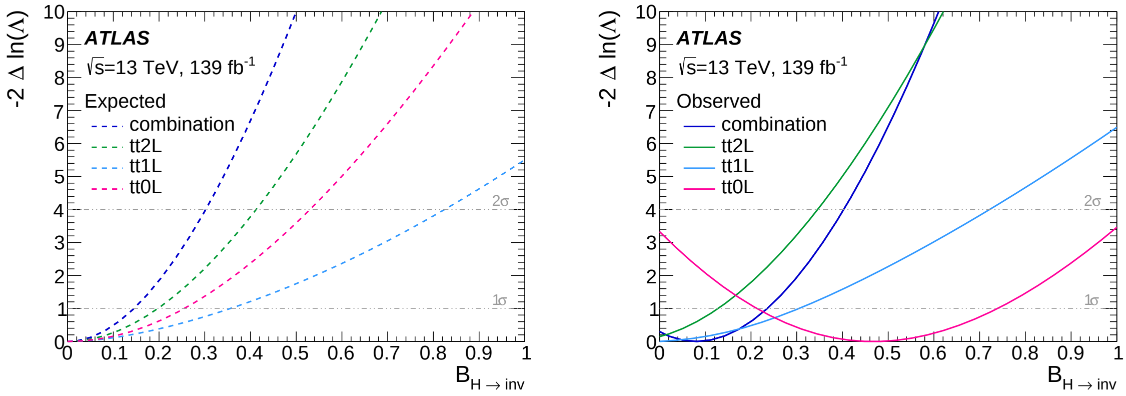

(a)

(b)

Figure 6: (a) The expected negative logarithmic profile likelihood ratios $-2\,\Delta\ln(\Lambda)$ as a function of $\mathcal{B}_{H\to\mathrm{inv}}$ for each of the three channels and their statistical combination and (b) these likelihood ratios for the observed data.

Table 3: Summary of results from direct searches for invisible decays of the 125 GeV Higgs boson in the $t\bar{t}H$ topology using 139 fb^{-1} of Run 2 data, and their statistical combination. Shown are the best-fit values of $\mathcal{B}_{H\to\mathrm{inv}}$, computed as not being bounded below by zero, for consistency with previous results [114]. Observed and expected upper limits on $\mathcal{B}_{H\to\mathrm{inv}}$ at the 95% CL are computed with the CL$_s$ method and are new results with respect to the individual analysis papers quoted in the last table column. The corresponding Asimov datasets for the expected results are constructed using nuisance parameter values from a fit to data with $\mathcal{B}_{H\to\mathrm{inv}} = 0$, and the quoted uncertainty corresponds to the 68% confidence interval.

Analysis	Best fit $\mathcal{B}_{H\to\mathrm{inv}}$	Observed upper limit	Expected upper limit	Reference
tt0L	$0.48^{+0.27}_{-0.27}$	0.95	$0.52^{+0.23}_{-0.16}$	[28], this document
tt1L	$-0.04^{+0.35}_{-0.29}$	0.74	$0.80^{+0.40}_{-0.26}$	[29], this document
tt2L	$-0.08^{+0.20}_{-0.19}$	0.36	$0.40^{+0.18}_{-0.12}$	[30], this document
$t\bar{t}H$ comb.	$0.08^{+0.15}_{-0.15}$	0.38	$0.30^{+0.13}_{-0.09}$	This document

6 Conclusion

In summary, a statistical combination of three analyses using 139 fb^{-1} of pp collisions delivered by the LHC at a centre-of-mass energy of 13 TeV and collected by the ATLAS detector is presented. The three analyses are all designed to select events with two top quarks and invisible particles, and consider all possible light lepton multiplicities arising from the decays of the two top quarks.

The statistical combination is used to set 95% confidence-level constraints on spin-0 simplified dark matter models. All production modes with top quarks in the final state (DM+$t\bar{t}$, DM+t) are considered. For scalar (pseudoscalar) dark matter models, the combination extends the excluded mass range by 50 (25) GeV beyond that of the best of the individual channels, excluding mediator masses up to 370 GeV with all couplings set to unity. In addition, the combination improves the observed coupling exclusion limit by 24%, assuming a pseudoscalar mediator mass of 10 GeV.

The specific case where the mediator corresponds to the SM 125 GeV Higgs boson is also considered when interpreting the results presented in this paper. An upper limit on the Higgs boson invisible branching ratio of 0.38 ($0.30^{+0.13}_{-0.09}$) is observed (expected) at 95% confidence level.

Appendix

A The tt0L-low analysis

The tt0L-low analysis aims to enhance the sensitivity to DM+$t\bar{t}$ signals with low mediator masses ($m(\phi), m(a) < 100$ GeV). Two main discriminating variables, $\cosh_{\text{max}}$ and $\chi^2_{t\bar{t},\,\text{had}}$, are defined in order to reduce the most dominant top quark backgrounds. Angular separations between b-tagged jets, $E_{\text{T}}^{\text{miss}}$ or large-radius jets are used to further reduce the contamination from Standard Model processes. To ensure orthogonality with the tt0L-high selections, additional orthogonalisation requirements are also applied, as detailed in Section 3.1.

A.1 Discriminating variables

The full event selections performed in the signal regions can be found in Table 1. The discriminating variables are described in more detail below.

cosh$_{\text{max}}$

The $\cosh_{\text{max}}$ variable is designed to distinguish signal events from single-top events in the tW channel and $t\bar{t}$ events with a lepton missed by the reconstruction algorithms (top-with-lost-lepton), which are among the main backgrounds in the analysis. Such events may enter the signal regions because of high $E_{\text{T}}^{\text{miss}}$ originating from the $t \to bW \to b\ell\nu$ decay, and the lost lepton.

The reconstruction of events containing a top quark with a lost lepton is attempted by assuming that the $E_{\text{T}}^{\text{miss}}$ is equal to the p_{T} of the leptonically decaying W boson with a lost lepton, $E_{\text{T}}^{\text{miss}} \sim p_{\text{T}}^{W}$.

The top-with-lost-lepton background can then be reconstructed by combining the missing transverse momentum with the correct b-tagged jet ($t \to bW$). In practice, a four-vector with p_{T} and ϕ corresponding to the $\boldsymbol{p}_{\text{T}}^{\text{miss}}$ vector and its mass equal to the W boson mass is built, while its pseudorapidity η_W (or equivalently p_z^W) remains unknown. Choosing the x-axis to be in the direction of p_{T}^{W} and adopting (E, p_x, p_y, p_z) coordinates:

$$\boldsymbol{p}_W = \left(\sqrt{(p_{\text{T}}^{W})^2 + (p_z^{W})^2 + m_W^2}, p_{\text{T}}^{W}, 0, p_z^{W}\right), \tag{1}$$

$$\boldsymbol{p}_b = \left(\sqrt{(p_{\text{T}}^{b})^2 + (p_z^{b})^2 + m_b^2}, p_{\text{T}}^{b} \cdot \cos(\phi_W - \phi_b), p_{\text{T}}^{b} \cdot \sin(\phi_W - \phi_b), p_z^{b}\right), \tag{2}$$

$$m_t^2 = (\boldsymbol{p}_W + \boldsymbol{p}_b)^2, \tag{3}$$

where the b superscript and subscript refer to one of the selected b-tagged jets. Substituting Eqs. (1) and (2) in Eq. (3), and assuming the massless limit for the b-tagged jet, the equivalence below is formed:

$$\sqrt{1+\left(\frac{m_W}{p_{\mathrm{T}}^{W}\cdot\cosh\eta_W}\right)^2}\cdot\cosh\eta_W\cdot\cosh\eta_b-\sinh\eta_W\cdot\sinh\eta_b=\frac{m_t^2-m_W^2}{2p_{\mathrm{T}}^{W}p_{\mathrm{T}}^{b}}+\cos(\phi_W-\phi_b), \tag{4}$$

where η_W is unknown. Given that $E_{\mathrm{T}}^{\mathrm{miss}} \sim p_{\mathrm{T}}^{W} > 160$ GeV in the signal regions and $\cosh\eta_W \geq 1$, it may be assumed that $m_W \sim 80\ \mathrm{GeV} \ll p_{\mathrm{T}}^{W}\cdot\cosh\eta_W$, such that:

$$\sqrt{1+\left(\frac{m_W}{p_{\mathrm{T}}^{W}\cdot\cosh\eta_W}\right)^2}\sim 1.$$

Equation (4) can thus be simplified:

$$\begin{aligned}\cosh(\eta_W-\eta_b) &\sim \frac{m_t^2-m_W^2}{2p_{\mathrm{T}}^{W}p_{\mathrm{T}}^{b}}+\cos(\phi_W-\phi_b) \\ &\sim \frac{m_t^2-m_W^2}{2E_{\mathrm{T}}^{\mathrm{miss}}p_{\mathrm{T}}^{b}}+\cos(\phi_{E_{\mathrm{T}}^{\mathrm{miss}}}-\phi_b).\end{aligned} \tag{5}$$

By definition, $\cosh(x) \geq 1$ so that the right-hand side of Eq. (5) is expected to be larger than 1 in the case of successful leptonic top reconstruction. The discriminating observable $\cosh_{\mathrm{max}}$ is therefore defined as:

$$\cosh_{\mathrm{max}} = \max\{\cosh\Delta\eta^1_{W,b}, \cosh\Delta\eta^2_{W,b}\},$$

where $\Delta\eta^1_{W,b}$ and $\Delta\eta^2_{W,b}$ represent the pseudorapidity difference between the W boson candidate and either of the two leading b-tagged jets selected in the event. Events with high $\cosh_{\mathrm{max}}$ values are likely to contain a top quark with a lost lepton and are excluded from the signal regions.

Figure 7 illustrates the modelling of the shape of $\cosh_{\mathrm{max}}$ in SRWX and SRTX. The $\cosh_{\mathrm{max}}$ distribution in SR0X is shown in Figure 3.

$\chi^2_{t\bar{t},\,\mathrm{had}}$

The $\chi^2_{t\bar{t},\,\mathrm{had}}$ observable approximately quantifies how likely an event is to include two hadronically decaying top quarks. It is used primarily to reject backgrounds containing no hadronic top quark decays, such as Z+jets events. It is defined as follows:

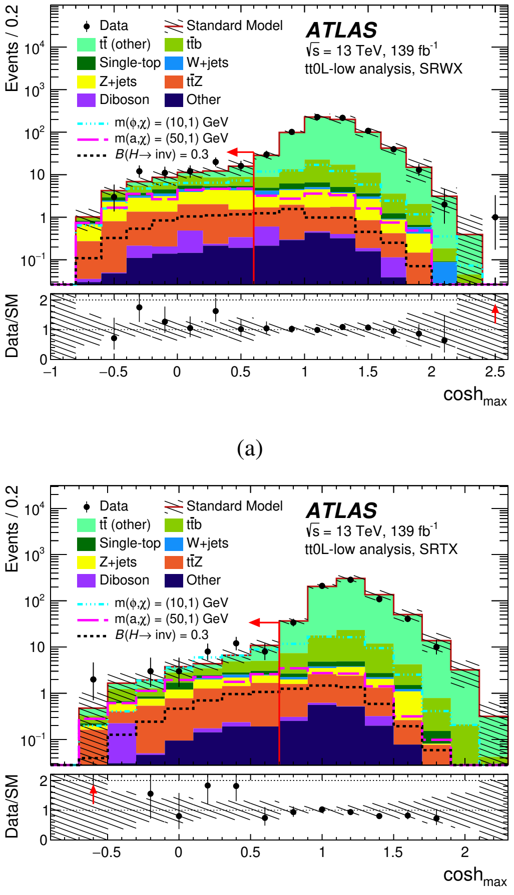

(a)

(b)

Figure 7: Distributions of $\cosh_{\max}$ in (a) SRWX and (b) SRTX events passing all the SR requirements except those on $\cosh_{\max}$ itself (which are indicated by the arrows). The contributions from all SM backgrounds are shown after the profile likelihood simultaneous fit to all tt0L-low CRs, with the hatched bands representing the total uncertainty. The category '$t\bar{t}$ (other)' represents $t\bar{t}$ events without extra jets or events with extra light-flavour jets. 'Other' includes contributions from $t\bar{t}$+W, tZ and tWZ processes. The expected distributions for selected signal models are shown as dashed lines. The underflow (overflow) events are included in the first (last) bin. The bottom panels show the ratio of the observed data to the total SM background prediction, with the hatched area representing the total uncertainty in the background prediction and the red arrows marking data outside the vertical-axis range.

$$\begin{aligned}\chi^2_{t\bar{t},\,\mathrm{had}} = &\left(\frac{m_{W_1} - m_{W_{\mathrm{ref}}}}{\sigma_{m_W}}\right)^2 \\ &+ \left(\frac{(m_{t_1} - m_{W_1}) - (m_{t_{\mathrm{ref}}} - m_{W_{\mathrm{ref}}})}{\sigma_{m_t - m_W}}\right)^2 \\ &+ \left(\frac{(m_{t_2} - m_{W_2}) - (m_{t_{\mathrm{ref}}} - m_{W_{\mathrm{ref}}})}{\sigma_{m_t - m_W}}\right)^2 .\end{aligned} \tag{6}$$

Up to seven jets, including the two selected b-tagged jets, are considered in the calculation. The first W boson candidate, W_1, is built from two non-b-tagged jets, while the first top quark candidate, t_1, combines W_1 and one of the b-tagged jets, b_1, such that $t_1 \rightarrow W_1 b_1$. According to Monte Carlo simulations, the second W boson candidate, W_2, is in more than 50% of the cases too soft to lead to two individual jets satisfying the reconstruction criteria. Hence, it is built from a single non-b-tagged jet to which the mass of the W boson is attributed. As a result, the second top quark candidate, $t_2 \rightarrow W_2 b_2$, contains only one non-b-tagged jet and the remaining b-tagged jet, b_2.

The first term in Eq. (6) corresponds to the invariant mass constraint from W_1. The values $m_{W_{\mathrm{ref}}}$ and σ_{m_W} are respectively the mean and the standard deviation of the experimental invariant mass distribution expected for hadronically decaying W bosons. The second and third terms correspond to the invariant mass constraints from t_1 and t_2, respectively. Since m_{W_1} and m_{t_1} (m_{W_2} and m_{t_2}) are strongly correlated, the W boson mass is subtracted from the top quark mass to decouple these two terms from the first one. The values of $m_{t_{\mathrm{ref}}}$ and $\sigma_{m_t - m_W}$ are respectively the mean of the experimental top quark mass distribution and the standard deviation of the $m_t - m_W$ distribution expected for reconstructed hadronic top quark decays. The values of $m_{W_{\mathrm{ref}}}$, σ_{m_W}, $m_{t_{\mathrm{ref}}}$ and $\sigma_{m_t - m_W}$ are taken from Ref. [116]:

- $m_{W_{\mathrm{ref}}} = 80.51$ GeV, $\sigma_{m_W} = 12.07$ GeV,
- $m_{t_{\mathrm{ref}}} - m_{W_{\mathrm{ref}}} = 85.17$ GeV, $\sigma_{m_t - m_W} = 16.05$ GeV.

The χ^2 is recomputed for each possible jet combination and the final $\chi^2_{t\bar{t},\,\mathrm{had}}$ corresponds to the minimum value obtained. Events with high $\chi^2_{t\bar{t},\,\mathrm{had}}$ values are less likely to contain two hadronic top quark decays and are therefore excluded from the signal regions.

Figure 8 illustrates the modelling of the shape of $\chi^2_{t\bar{t},\,\mathrm{had}}$ in SRWX and SRTX. The $\chi^2_{t\bar{t},\,\mathrm{had}}$ distribution in SR0X is shown in Figure 3.

A.2 Background estimation

The event topologies in the signal regions and control regions are kept as similar as possible to reduce any bias originating from differences between their kinematic phase spaces. For this purpose, control regions with one or more leptons in the final state are split according to the mass of the heaviest large-radius jet, as is done for the signal regions, while all $E_{\mathrm{T}}^{\mathrm{miss}}$-related variables are recalculated by treating the selected leptons as invisible, denoted by the subscript 'no lepton' in the variable names.

One of the most prominent sources of background in the signal regions is semileptonic $t\bar{t}$ decay where the lepton is misreconstructed or outside the detector acceptance, while the contribution from the dileptonic $t\bar{t}$ decay is negligible. Control regions selecting events with exactly one lepton (e or μ) are defined in order to estimate the background originating from a top quark decay with a lost lepton, which includes single-top events in the tW channel, and $t\bar{t}$+b and $t\bar{t}$ (other) events.

A χ^2-based observable [117], $\chi^2_{t\bar{t},\,\mathrm{lep}}$, taking into account the kinematic properties of $E_{\mathrm{T}}^{\mathrm{miss}}$, lepton, jets and the b-tagging information, is used to reconstruct semileptonic $t\bar{t}$ events and separate them from tW and $t\bar{t}$+b events. It follows an approach similar to that for the $\chi^2_{t\bar{t},\,\mathrm{had}}$ variables by placing constraints on the masses of the hadronically decaying W boson, the hadronically decaying top quark and the leptonically decaying top quark. The presence of extra b-tagged jets is used to select $t\bar{t}$+b over single-top processes. Tighter $\cosh_{\mathrm{max,\,no\ lepton}}$ selections are required in the single-top control regions to reduce the contamination

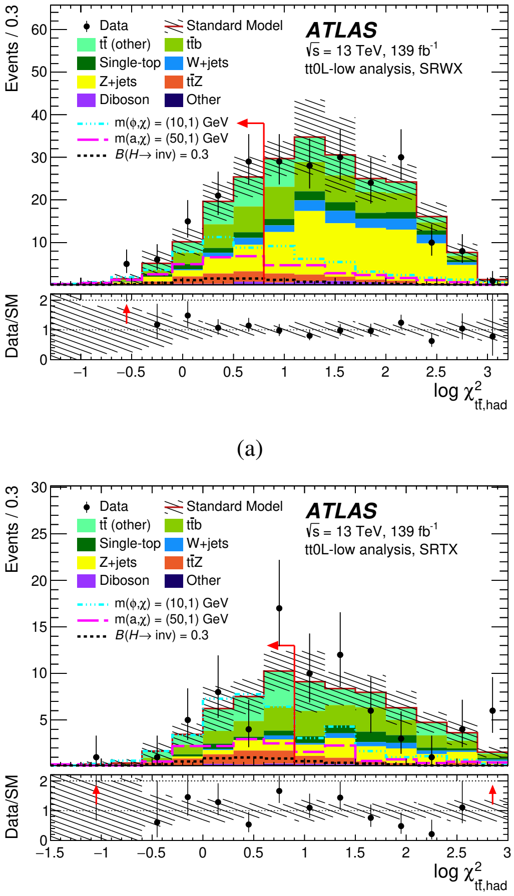

(a)

(b)

Figure 8: Distributions of $\chi^2_{t\bar{t},\,\mathrm{had}}$ in (a) SRWX and (b) SRTX events passing all the SR requirements except those on $\chi^2_{t\bar{t},\,\mathrm{had}}$ itself (which are indicated by the arrows). The contributions from all SM backgrounds are shown after the profile likelihood simultaneous fit to all tt0L-low CRs, with the hatched bands representing the total uncertainty. The category '$t\bar{t}$ (other)' represents $t\bar{t}$ events without extra jets or events with extra light-flavour jets. 'Other' includes contributions from $t\bar{t}$+W, tZ and tWZ processes. The expected distributions for selected signal models are shown as dashed lines. The underflow (overflow) events are included in the first (last) bin. The bottom panels show the ratio of the observed data to the total SM background prediction, with the hatched area representing the total uncertainty in the background prediction and the red arrows marking data outside the vertical-axis range.

from semileptonic $t\bar{t}$ events failing the $\chi^2_{t\bar{t},\,\mathrm{lep}}$ reconstruction and attain high purity in tW events. Table 4 presents the full event selections applied to define the top-with-lost-lepton control regions.

Another major background component in the signal regions contains $Z \rightarrow \nu\nu$ produced in association with jets. Control regions selecting events with two leptons with opposite charge and the same flavour (ee or $\mu\mu$) are defined in order to estimate the $Z(\nu\nu)$+jets background. The invariant mass and transverse momentum of the dilepton system, $m_{\ell\ell}$ and $p_{\mathrm{T}}^{\ell\ell}$ respectively, and the missing transverse momentum significance $\mathcal{S}$ serve as the major discriminants to suppress the contamination from dileptonic $t\bar{t}$ events. To obtain enough events, several selections applied in the signal regions are omitted in the corresponding CRs. Table 5 presents the full event selections applied to define the Z+jets control regions.

Table 4: Selection criteria for the top-with-lost-lepton control regions used in the tt0L-low analysis.

	Variables	**CR0X**	**CRWX**	**CRTX**
Shared selections	N_{lepton}	= 1		
	$E_{\text{T, no lepton}}^{\text{miss}}$ [GeV]	> 160		
	$E_{\text{T}}^{\text{miss}}$ [GeV]	< 250, when passing b-jet triggers		
	$\mathcal{S}_{\text{no lepton}}$	> 10		
	$\Delta\phi_{\text{min}}(\boldsymbol{p}_{\text{T},1\text{-}4}, \boldsymbol{p}_{\text{T,no lepton}}^{\text{miss}})$	> 1.0	> 0.5	
	$\Delta R\,(b_1, b_2)$	> 1.2		
	$N_{\text{large-radius jet}}$	= 0	> 0	
	$m_{\text{large-radius jet}}$ [GeV]	—	(40, 130)	≥ 130
	ΔR_{min}(large-radius jet, b-tagged jets)	—		< 1.2
	$\cosh_{\text{max, no lepton}}$	< 0.9	< 0.95	< 1.0
	$\chi^2_{t\bar{t},\text{ had}}$	< 10	< 20	< 40
	$p_{\text{T}}^{t\bar{t}}/E_{\text{T, no lepton}}^{\text{miss}}$	(0.7, 1.2)	(0.5, 1.2)	
$t\bar{t}$ (other) enriched selections	**Variables**	**CR0X**$_{t\bar{t}}$	**CRWX**$_{t\bar{t}}$	**CRTX**$_{t\bar{t}}$
	$\chi^2_{t\bar{t},\text{ lep}}$	< 6		
$t\bar{t}$+b enriched selections	**Variables**	**CR0X**$_{t\bar{t}+b}$	**CRWX**$_{t\bar{t}+b}$	**CRTX**$_{t\bar{t}+b}$
	$\chi^2_{t\bar{t},\text{ lep}}$	≥ 6		
	$N_{\text{extra }b\text{-tagged jet}}$	≥ 1		
Single-top enriched selections	**Variables**	**CR0X**$_{\text{single-top}}$	**CRWX**$_{\text{single-top}}$	**CRTX**$_{\text{single-top}}$
	$\chi^2_{t\bar{t},\text{ lep}}$	≥ 30		
	$N_{\text{extra }b\text{-tagged jet}}$	= 0		
	$\cosh_{\text{max, no lepton}}$	< 0.5	< 0.6	< 0.7

Table 5: Selection criteria for the Z+jets control regions used in the tt0L-low analysis.

Variables	**CR0X**$_{Z\text{+jets}}$	**CRWX**$_{Z\text{+jets}}$	**CRTX**$_{Z\text{+jets}}$
N_{lepton}	= 2		
Orthogonalisation	$\text{N}^{R=1.2}_{\text{large-radius jet}} < 2$ or $m^{R=1.2}_{\text{subleading large-radius jet}} < 60$ GeV		
$E_{\text{T, no lepton}}^{\text{miss}}$ [GeV]	> 160		
$\mathcal{S}_{\text{no lepton}}$	> 8		
$\Delta\phi_{\text{min}}(\boldsymbol{p}_{\text{T},1\text{-}4}, \boldsymbol{p}_{\text{T}}^{\text{miss}})$	> 0.5		
$N_{\text{large-radius jet}}$	= 0	> 0	
$m_{\text{large-radius jet}}$ [GeV]	—	(40, 130)	≥ 130
$m_{\ell\ell}$ [GeV]	(80, 100)		
$p_{\text{T}}^{\ell\ell}$ [GeV]	> 160		
$\mathcal{S}$	< 5		

Validation regions are not included in the statistical model and serve only to validate the extrapolation over lepton multiplicity when going from the control regions to the signal regions. The event selections for the validation regions therefore require zero leptons, while being orthogonal to the signal region selections.

In the $t\bar{t}$-enriched validation regions, $t\bar{t}$ events are selected by inverting the tight $\cosh_{\text{max}}$ requirement applied in the signal regions and adding a looser upper bound. The validation regions for $t\bar{t}$+b, single-top and Z+jets are merged into a single $t\bar{t}$-suppressed validation region because of the limited number of events in the 0-lepton phase space. In these regions the $\chi^2_{t\bar{t},\,\mathrm{had}}$ selection applied in the signal regions is inverted. The $p_{\mathrm{T}}^{t\bar{t}}/E_{\mathrm{T}}^{\mathrm{miss}}$ requirements are discarded because they become irrelevant when the value of $\chi^2_{t\bar{t},\,\mathrm{had}}$ is too large. Tight $\Delta R\left(b_1, b_2\right)$ selections are imposed to minimise the contamination from W+jets events, with their thresholds optimised in each region to provide a number of events similar to that in the $t\bar{t}$-enriched VRs. All the background predictions in the VRs agree with the data to within 1σ.

A.3 Results

All tt0L-low signal and control regions are included in a statistical model based on the combined likelihood fit. The normalisations of the $t\bar{t}$+b, $t\bar{t}$ (other), single-top and Z+jets background processes are free-floating. For the $t\bar{t}$ background, the normalisation factors are decorrelated in the three kinematic regimes (CR0X, CRWX and CRTX) to account for a possible top quark p_{T} dependence of the normalisation factor. The yield results are presented in Table 2.

Figure 9 shows the $E_{\mathrm{T}}^{\mathrm{miss}}$ distributions in the three tt0L-low signal regions. The background contributions are obtained from the profile likelihood simultaneous fit to all tt0L-low CRs with a background-only hypothesis.

Exclusion limits at 95% CL are presented in Figures 10(a) and 10(b) for DM models with a spin-0 scalar or pseudoscalar mediator particle, respectively. The tt0L-low analysis, the tt0L-high analysis and the full tt0L combination are presented separately in order to quantify the improvement gained by adding the tt0L-low channel to the tt0L search. As they were designed to do, the tt0L-low signal regions extend the sensitivity to low-mass mediator models, with an improvement of up to about 15% in the cross-section limit for scalar mediator particles.

In addition, the negative logarithmic profile likelihood ratios $-2\,\Delta\ln(\Lambda)(\mathcal{B}_{H\to\mathrm{inv}};\theta)$ as a function of $\mathcal{B}_{H\to\mathrm{inv}}$ for the tt0L-low and tt0L-high analyses, and their combination, are illustrated in Figure 11.

Table 6 presents the best-fit value, and the observed and expected upper limits on $\mathcal{B}_{H\to\mathrm{inv}}$ at the 95% CL for the tt0L-low analysis, the tt0L-high analysis and their statistical combination. Since the tt0L-low selection was designed to target mediator masses below 100 GeV, the improvement in the expected upper limit at the Higgs boson mass is found to be relatively small.

Table 6: Results from the tt0L-low and tt0L-high searches for invisible decays of the 125 GeV Higgs boson in the $t\bar{t}H$ topology using 139 fb^{-1} of Run 2 data, and their statistical combination. Shown are the best-fit values of $\mathcal{B}_{H\to\mathrm{inv}}$, as well as observed and expected upper limits on $\mathcal{B}_{H\to\mathrm{inv}}$ at the 95% CL. The corresponding Asimov datasets for the expected results are constructed using nuisance parameter values from a fit to data with $\mathcal{B}_{H\to\mathrm{inv}} = 0$, and the quoted uncertainty corresponds to the 68% confidence interval.

Analysis	Best fit $\mathcal{B}_{H\to\mathrm{inv}}$	Observed upper limit	Expected upper limit	Reference
tt0L-low	$0.88^{+0.48}_{-0.46}$	1.80	$1.09^{+0.50}_{-0.26}$	this document
tt0L-high	$0.27^{+0.28}_{-0.27}$	0.80	$0.59^{+0.29}_{-0.18}$	[28], this document
tt0L comb.	$0.48^{+0.27}_{-0.27}$	0.95	$0.52^{+0.23}_{-0.16}$	[28], this document

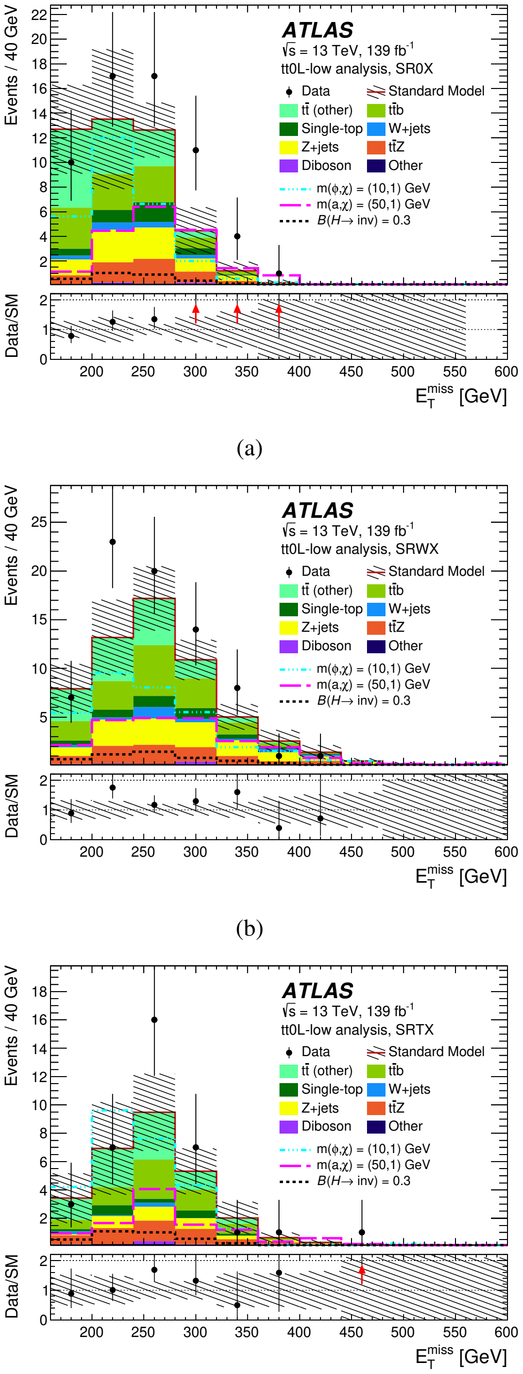

(a)

(b)

(c)

Figure 9: $E_{\mathrm{T}}^{\mathrm{miss}}$ distributions in (a) SR0X, (b) SRWX and (c) SRTX events passing all the SR requirements. The contributions from all SM backgrounds are shown after the profile likelihood simultaneous fit to all tt0L-low CRs, with the hatched bands representing the total uncertainty. The category '$t\bar{t}$ (other)' represents $t\bar{t}$ events without extra jets or events with extra light-flavour jets. 'Other' includes contributions from $t\bar{t}$+W, tZ and tWZ processes. The expected distributions for selected signal models are shown as dashed lines. The overflow events are included in the last bin. The bottom panels show the ratio of the observed data to the total SM background prediction, with the hatched area representing the total uncertainty in the background prediction and the red arrows marking data outside the vertical-axis range.

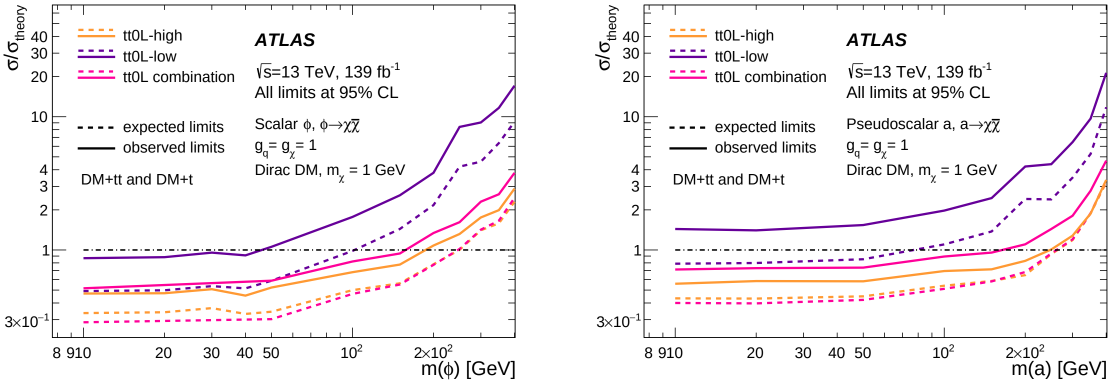

(a) (b)

Figure 10: Exclusion limits for colour-neutral (a) scalar or (b) pseudoscalar mediator dark matter models as a function of the mediator mass $m(\phi)$ or $m(a)$ for a DM mass $m_\chi = 1$ GeV. Associated production of DM with both single top quarks (tW and tj channels) and top quark pairs is considered. The limits are calculated at 95% CL and are expressed in terms of the ratio of the excluded cross section to the nominal cross section for a coupling assumption of $g = g_q = g_\chi = 1$. The solid (dashed) lines show the observed (expected) exclusion limits for the tt0L-high and tt0L-low analyses and their statistical combination.

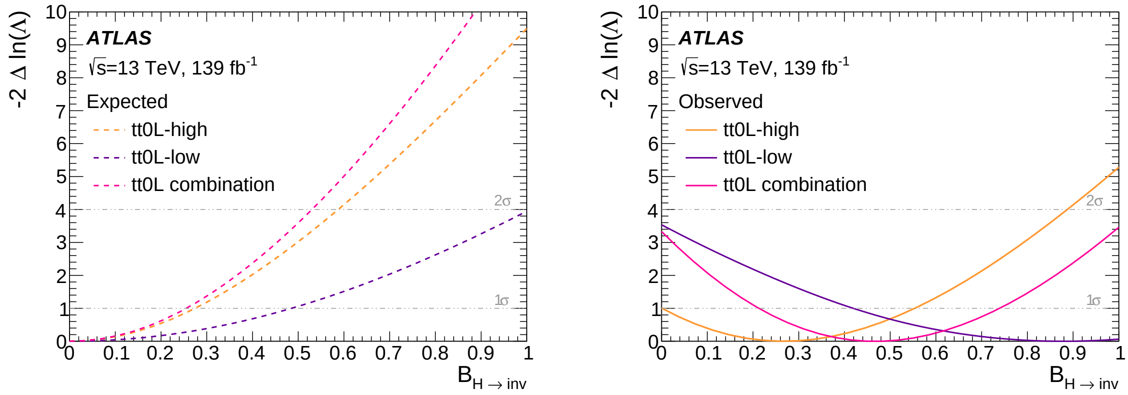

(a) (b)

Figure 11: (a) The expected negative logarithmic profile likelihood ratios $-2\,\Delta\ln(\Lambda)$ as a function of $\mathcal{B}_{H\to\text{inv}}$ for each of the two tt0L analyses and their statistical combination and (b) these likelihood ratios for the observed data.

References

[1] F. Zwicky, *Die Rotverschiebung von extragalaktischen Nebeln*, Helv. Phys. Acta **6** (1933) 110.

[2] G. Bertone, D. Hooper and J. Silk, *Particle dark matter: Evidence, candidates and constraints*, Phys. Rept. **405** (2005) 279, arXiv: `hep-ph/0404175`.

[3] E. Komatsu et al., *Seven-Year Wilkinson Microwave Anisotropy Probe (WMAP) Observations: Cosmological Interpretation*, Astrophys. J. Suppl. **192** (2011) 18, arXiv: `1001.4538 [astro-ph.CO]`.

[4] Planck Collaboration, *Planck 2015 results. XIII. Cosmological parameters*, Astron. Astrophys. **594** (2016) A13, arXiv: `1502.01589 [astro-ph.CO]`.

[5] G. Steigman and M. S. Turner, *Cosmological Constraints on the Properties of Weakly Interacting Massive Particles*, Nucl. Phys. B **253** (1985) 375.

[6] ATLAS Collaboration, *Search for new phenomena in events with an energetic jet and missing transverse momentum in pp collisions at $\sqrt{s} = 13$ TeV with the ATLAS detector*, Phys. Rev. D **103** (2021) 112006, arXiv: `2102.10874 [hep-ex]`.

[7] CMS Collaboration, *Search for dark matter produced in association with a leptonically decaying Z boson in proton–proton collisions at $\sqrt{s} = 13$ TeV*, Eur. Phys. J. C **81** (2021) 13, arXiv: `2008.04735 [hep-ex]`.

[8] ATLAS Collaboration, *Search for new phenomena in final states with b-jets and missing transverse momentum in $\sqrt{s} = 13$ TeV pp collisions with the ATLAS detector*, JHEP **05** (2021) 093, arXiv: `2101.12527 [hep-ex]`.

[9] ATLAS Collaboration, *Search for dark matter in association with an energetic photon in pp collisions at $\sqrt{s} = 13$ TeV with the ATLAS detector*, JHEP **02** (2021) 226, arXiv: `2011.05259 [hep-ex]`.

[10] ATLAS Collaboration, *Search for dark matter produced in association with bottom or top quarks in $\sqrt{s} = 13$ TeV pp collisions with the ATLAS detector*, Eur. Phys. J. C **78** (2018) 18, arXiv: `1710.11412 [hep-ex]`.

[11] ATLAS Collaboration, *Search for dark matter produced in association with a Standard Model Higgs boson decaying into b-quarks using the full Run 2 dataset from the ATLAS detector*, JHEP **11** (2021) 209, arXiv: `2108.13391 [hep-ex]`.

[12] ATLAS Collaboration, *Constraints on mediator-based dark matter and scalar dark energy models using $\sqrt{s} = 13$ TeV pp collision data collected by the ATLAS detector*, JHEP **05** (2019) 142, arXiv: `1903.01400 [hep-ex]`.

[13] A. Boveia et al., *Recommendations on presenting LHC searches for missing transverse energy signals using simplified s-channel models of dark matter*, Phys. Dark Univ. **27** (2020) 100365, arXiv: `1603.04156 [hep-ex]`.

[14] A. Albert et al., *Recommendations of the LHC Dark Matter Working Group: Comparing LHC searches for dark matter mediators in visible and invisible decay channels and calculations of the thermal relic density*, Phys. Dark Univ. **26** (2019) 100377, arXiv: `1703.05703 [hep-ex]`.

[15] T. Abe et al., *LHC Dark Matter Working Group: Next-generation spin-0 dark matter models*, Phys. Dark Univ. **27** (2020) 100351, arXiv: `1810.09420 [hep-ex]`.

[16] D. Abercrombie et al., *Dark Matter benchmark models for early LHC Run-2 Searches: Report of the ATLAS/CMS Dark Matter Forum*, Phys. Dark Univ. **27** (2020) 100371, arXiv: `1507.00966 [hep-ex]`.

[17] M. Blanke, P. Pani, G. Polesello and G. Rovelli, *Single-top final states as a probe of top-flavoured dark matter models at the LHC*, JHEP **01** (2021) 194, arXiv: `2010.10530 [hep-ph]`.

[18] S. Westhoff, *New physics searches with top quarks*, PoS **LeptonPhoton2019** (2019) 012, arXiv: `1912.02054 [hep-ph]`.

[19] U. Haisch and G. Polesello, *Searching for production of dark matter in association with top quarks at the LHC*, JHEP **02** (2019) 029, arXiv: `1812.00694 [hep-ph]`.

[20] U. Haisch, P. Pani and G. Polesello, *Determining the CP nature of spin-0 mediators in associated production of dark matter and $t\bar{t}$ pairs*, JHEP **02** (2017) 131, arXiv: `1611.09841 [hep-ph]`.

[21] U. Haisch and E. Re, *Simplified dark matter top-quark interactions at the LHC*, JHEP **06** (2015) 078, arXiv: `1503.00691 [hep-ph]`.

[22] J. Abdallah et al., *Simplified Models for Dark Matter Searches at the LHC*, Phys. Dark Univ. **9-10** (2015) 8, arXiv: `1506.03116 [hep-ph]`.

[23] M. R. Buckley, D. Feld and D. Goncalves, *Scalar simplified models for dark matter*, Phys. Rev. D **91** (2015) 015017, arXiv: `1410.6497 [hep-ph]`.

[24] G. D'Ambrosio, G. F. Giudice, G. Isidori and A. Strumia, *Minimal flavour violation: an effective field theory approach*, Nucl. Phys. B **645** (2002) 155, arXiv: `hep-ph/0207036`.

[25] M. Backovic et al., *Higher-order QCD predictions for dark matter production at the LHC in simplified models with s-channel mediators*, Eur. Phys. J. C **75** (2015) 482, arXiv: `1508.05327 [hep-ph]`.

[26] D. Pinna, A. Zucchetta, M. R. Buckley and F. Canelli, *Single top quarks and dark matter*, Phys. Rev. D **96** (2017) 035031, arXiv: `1701.05195 [hep-ph]`.

[27] P. Pani and G. Polesello, *Dark matter production in association with a single top-quark at the LHC in a two-Higgs-doublet model with a pseudoscalar mediator*, Phys. Dark Univ. **21** (2018) 8, arXiv: `1712.03874 [hep-ph]`.

[28] ATLAS Collaboration, *Search for a scalar partner of the top quark in the all-hadronic $t\bar{t}$ plus missing transverse momentum final state at $\sqrt{s} = 13$ TeV with the ATLAS detector*, Eur. Phys. J. C **80** (2020) 737, arXiv: `2004.14060 [hep-ex]`.

[29] ATLAS Collaboration, *Search for new phenomena with top quark pairs in final states with one lepton, jets, and missing transverse momentum in pp collisions at $\sqrt{s} = 13$ TeV with the ATLAS detector*, JHEP **04** (2020) 174, arXiv: `2012.03799 [hep-ex]`.

[30] ATLAS Collaboration, *Search for new phenomena in events with two opposite-charge leptons, jets and missing transverse momentum in pp collisions at $\sqrt{s} = 13$ TeV with the ATLAS detector*, JHEP **04** (2021) 165, arXiv: `2102.01444 [hep-ex]`.

[31] ATLAS Collaboration, *The ATLAS Experiment at the CERN Large Hadron Collider*, JINST **3** (2008) S08003.

[32] ATLAS Collaboration, *ATLAS Insertable B-Layer Technical Design Report*, ATLAS-TDR-19; CERN-LHCC-2010-013, 2010, URL: `https://cds.cern.ch/record/1291633`, Addendum: ATLAS-TDR-19-ADD-1; CERN-LHCC-2012-009, 2012, URL: `https://cds.cern.ch/record/1451888`.

[33] ATLAS Collaboration, *Configuration and performance of the ATLAS b-jet triggers in Run 2*, Eur. Phys. J. C **81** (2021) 1087, arXiv: `2106.03584 [hep-ex]`.

[34] ATLAS Collaboration, *Search for dark matter produced in association with a single top quark in $\sqrt{s} = 13$ TeV pp collisions with the ATLAS detector*, Eur. Phys. J. C **81** (2021) 860, arXiv: `2011.09308 [hep-ex]`.

[35] ATLAS Collaboration, *Observation of a new particle in the search for the Standard Model Higgs boson with the ATLAS detector at the LHC*, Phys. Lett. B **716** (2012) 1, arXiv: `1207.7214 [hep-ex]`.

[36] D. de Florian et al., *Handbook of LHC Higgs Cross Sections: 4. Deciphering the Nature of the Higgs Sector*, (2016), arXiv: `1610.07922 [hep-ph]`.

[37] R. E. Shrock and M. Suzuki, *Invisible Decays of Higgs Bosons*, Phys. Lett. B **110** (1982) 250.

[38] D. Choudhury and D. P. Roy, *Signatures of an invisibly decaying Higgs particle at LHC*, Phys. Lett. B **322** (1994) 368, arXiv: `hep-ph/9312347 [hep-ph]`.

[39] N. Arkani-Hamed, S. Dimopoulos, G. Dvali and J. March-Russell, *Neutrino masses from large extra dimensions*, Phys. Rev. D **65** (2001) 024032, arXiv: `hep-ph/9811448 [hep-ph]`.

[40] O. J. P. Eboli and D. Zeppenfeld, *Observing an invisible Higgs boson*, Phys. Lett. B **495** (2000) 147, arXiv: `hep-ph/0009158 [hep-ph]`.

[41] R. M. Godbole, M. Guchait, K. Mazumdar, S. Moretti and D. P. Roy, *Search for 'invisible' Higgs signals at LHC via associated production with gauge bosons*, Phys. Lett. B **571** (2003) 184, arXiv: `hep-ph/0304137 [hep-ph]`.

[42] I. Antoniadis, M. Tuckmantel and F. Zwirner, *Phenomenology of a leptonic goldstino and invisible Higgs boson decays*, Nucl. Phys. B **707** (2005) 215, arXiv: `hep-ph/0410165 [hep-ph]`.

[43] H. Davoudiasl, T. Han and H. E. Logan, *Discovering an invisibly decaying Higgs boson at hadron colliders*, Phys. Rev. D **71** (2005) 115007, arXiv: `hep-ph/0412269 [hep-ph]`.

[44] B. Patt and F. Wilczek, *Higgs-field portal into hidden sectors*, (2006), arXiv: `hep-ph/0605188 [hep-ph]`.

[45] S. Kanemura, S. Matsumoto, T. Nabeshima and N. Okada, *Can WIMP Dark Matter overcome the Nightmare Scenario?*, Phys. Rev. D **82** (2010) 055026, arXiv: `1005.5651 [hep-ph]`.

[46] A. Djouadi, O. Lebedev, Y. Mambrini and J. Quevillon, *Implications of LHC searches for Higgs–portal dark matter*, Phys. Lett. B **709** (2012) 65, arXiv: `1112.3299 [hep-ph]`.

[47] D. Ghosh, R. Godbole, M. Guchait, K. Mohan and D. Sengupta, *Looking for an Invisible Higgs Signal at the LHC*, Phys. Lett. B **725** (2013) 344, arXiv: `1211.7015 [hep-ph]`.

[48] G. Belanger, B. Dumont, U. Ellwanger, J. F. Gunion and S. Kraml, *Status of invisible Higgs decays*, Phys. Lett. B **723** (2013) 340, arXiv: `1302.5694 [hep-ph]`.

[49] D. Curtin et al., *Exotic decays of the 125 GeV Higgs boson*, Phys. Rev. D **90** (2014) 075004, arXiv: `1312.4992 [hep-ph]`.

[50] M. Zaazoua, L. Truong, K. A. Assamagan and F. Fassi, *Higgs portal vector dark matter interpretation: review of Effective Field Theory approach and ultraviolet complete models*, (2021), arXiv: `2107.01252 [hep-ph]`.

[51] ATLAS Collaboration,
Combination of Searches for Invisible Higgs Boson Decays with the ATLAS Experiment,
Phys. Rev. Lett. **122** (2019) 231801, arXiv: `1904.05105 [hep-ex]`.

[52] CMS Collaboration, *Search for invisible decays of a Higgs boson produced through vector boson fusion in proton–proton collisions at* $\sqrt{s} = 13$ *TeV*, Phys. Lett. B **793** (2019) 520,
arXiv: `1809.05937 [hep-ex]`.

[53] ATLAS Collaboration, *Search for invisible Higgs-boson decays in events with vector-boson fusion signatures using 139 fb*$^{-1}$ *of proton-proton data recorded by the ATLAS experiment*, (2022),
arXiv: `2202.07953 [hep-ex]`.

[54] CMS Collaboration, *Search for invisible decays of the Higgs boson produced via vector boson fusion in proton-proton collisions at* $\sqrt{s} = 13$ TeV, Phys. Rev. D **105** (9 2022) 092007,
arXiv: `2201.11585`.

[55] ATLAS Collaboration, *The ATLAS Collaboration Software and Firmware*,
ATL-SOFT-PUB-2021-001, 2021, URL: `https://cds.cern.ch/record/2767187`.

[56] ATLAS Collaboration, *Vertex Reconstruction Performance of the ATLAS Detector at* $\sqrt{s} = 13$ *TeV*,
ATL-PHYS-PUB-2015-026, 2015, URL: `https://cds.cern.ch/record/2037717`.

[57] ATLAS Collaboration, *Electron and photon performance measurements with the ATLAS detector using the 2015–2017 LHC proton–proton collision data*, JINST **14** (2019) P12006,
arXiv: `1908.00005 [hep-ex]`.

[58] ATLAS Collaboration, *Muon reconstruction performance of the ATLAS detector in proton–proton collision data at* $\sqrt{s} = 13$ *TeV*, Eur. Phys. J. C **76** (2016) 292, arXiv: `1603.05598 [hep-ex]`.

[59] ATLAS Collaboration, *Identification and energy calibration of hadronically decaying tau leptons with the ATLAS experiment in* pp *collisions at* $\sqrt{s} = 8$ *TeV*, Eur. Phys. J. C **75** (2015) 303,
arXiv: `1412.7086 [hep-ex]`.

[60] M. Cacciari, G. P. Salam and G. Soyez, *The anti-*k_t *jet clustering algorithm*, JHEP **04** (2008) 063,
arXiv: `0802.1189 [hep-ph]`.

[61] M. Cacciari, G. P. Salam and G. Soyez, *FastJet user manual*, Eur. Phys. J. C **72** (2012) 1896,
arXiv: `1111.6097 [hep-ph]`.

[62] B. Nachman, P. Nef, A. Schwartzman, M. Swiatlowski and C. Wanotayaroj,
Jets from Jets: Re-clustering as a tool for large radius jet reconstruction and grooming at the LHC,
JHEP **02** (2015) 075, arXiv: `1407.2922 [hep-ph]`.

[63] ATLAS Collaboration, *Jet reclustering and close-by effects in ATLAS Run 2*,
ATLAS-CONF-2017-062, 2017, URL: `https://cds.cern.ch/record/2275649`.

[64] ATLAS Collaboration, *Performance of b-jet identification in the ATLAS experiment*,
JINST **11** (2016) P04008, arXiv: `1512.01094 [hep-ex]`.

[65] ATLAS Collaboration, *Optimisation of the ATLAS b-tagging performance for the 2016 LHC Run*,
ATL-PHYS-PUB-2016-012, 2016, URL: `https://cds.cern.ch/record/2160731`.

[66] ATLAS Collaboration, *Performance of missing transverse momentum reconstruction with the ATLAS detector using proton–proton collisions at* $\sqrt{s} = 13$ *TeV*, Eur. Phys. J. C **78** (2018) 903,
arXiv: `1802.08168 [hep-ex]`.

[67] ATLAS Collaboration, *Performance of electron and photon triggers in ATLAS during LHC Run 2*,
Eur. Phys. J. C **80** (2020) 47, arXiv: `1909.00761 [hep-ex]`.

[68] ATLAS Collaboration, *Performance of the ATLAS muon triggers in Run 2*, JINST **15** (2020) P09015, arXiv: `2004.13447 [hep-ex]`.

[69] ATLAS Collaboration, *Performance of the missing transverse momentum triggers for the ATLAS detector during Run-2 data taking*, JHEP **08** (2020) 080, arXiv: `2005.09554 [hep-ex]`.

[70] ATLAS Collaboration, *Luminosity determination in pp collisions at $\sqrt{s} = 13$ TeV using the ATLAS detector at the LHC*, ATLAS-CONF-2019-021, 2019, URL: `https://cds.cern.ch/record/2677054`.

[71] G. Avoni et al., *The new LUCID-2 detector for luminosity measurement and monitoring in ATLAS*, JINST **13** (2018) P07017.

[72] ATLAS Collaboration, *ATLAS data quality operations and performance for 2015–2018 data-taking*, JINST **15** (2020) P04003, arXiv: `1911.04632 [physics.ins-det]`.

[73] ATLAS Collaboration, *The ATLAS Simulation Infrastructure*, Eur. Phys. J. C **70** (2010) 823, arXiv: `1005.4568 [physics.ins-det]`.

[74] GEANT4 Collaboration, S. Agostinelli et al., *GEANT4 – a simulation toolkit*, Nucl. Instrum. Meth. A **506** (2003) 250.

[75] T. Sjöstrand et al., *An introduction to PYTHIA 8.2*, Comput. Phys. Commun. **191** (2015) 159, arXiv: `1410.3012 [hep-ph]`.

[76] T. Sjöstrand, S. Mrenna and P. Skands, *A brief introduction to PYTHIA 8.1*, Comput. Phys. Commun. **178** (2008) 852, arXiv: `0710.3820 [hep-ph]`.

[77] R. D. Ball et al., *Parton distributions with LHC data*, Nucl. Phys. B **867** (2013) 244, arXiv: `1207.1303 [hep-ph]`.

[78] ATLAS Collaboration, *The Pythia 8 A3 tune description of ATLAS minimum bias and inelastic measurements incorporating the Donnachie–Landshoff diffractive model*, ATL-PHYS-PUB-2016-017, 2016, URL: `https://cds.cern.ch/record/2206965`.

[79] S. Frixione, G. Ridolfi and P. Nason, *A positive-weight next-to-leading-order Monte Carlo for heavy flavour hadroproduction*, JHEP **09** (2007) 126, arXiv: `0707.3088 [hep-ph]`.

[80] P. Nason, *A new method for combining NLO QCD with shower Monte Carlo algorithms*, JHEP **11** (2004) 040, arXiv: `hep-ph/0409146`.

[81] S. Frixione, P. Nason and C. Oleari, *Matching NLO QCD computations with parton shower simulations: the POWHEG method*, JHEP **11** (2007) 070, arXiv: `0709.2092 [hep-ph]`.

[82] S. Alioli, P. Nason, C. Oleari and E. Re, *A general framework for implementing NLO calculations in shower Monte Carlo programs: the POWHEG BOX*, JHEP **06** (2010) 043, arXiv: `1002.2581 [hep-ph]`.

[83] M. Czakon and A. Mitov, *Top++: A program for the calculation of the top-pair cross-section at hadron colliders*, Comput. Phys. Commun. **185** (2014) 2930, arXiv: `1112.5675 [hep-ph]`.

[84] T. Gleisberg et al., *Event generation with SHERPA 1.1*, JHEP **02** (2009) 007, arXiv: `0811.4622 [hep-ph]`.

[85] T. Gleisberg and S. Höche, *Comix, a new matrix element generator*, JHEP **12** (2008) 039, arXiv: `0808.3674 [hep-ph]`.

[86] F. Cascioli, P. Maierhöfer and S. Pozzorini, *Scattering Amplitudes with Open Loops*, Phys. Rev. Lett. **108** (2012) 111601, arXiv: `1111.5206 [hep-ph]`.

[87] S. Schumann and F. Krauss, *A parton shower algorithm based on Catani–Seymour dipole factorisation*, JHEP **03** (2008) 038, arXiv: `0709.1027 [hep-ph]`.

[88] S. Höche, F. Krauss, M. Schönherr and F. Siegert, *QCD matrix elements + parton showers. The NLO case*, JHEP **04** (2013) 027, arXiv: `1207.5030 [hep-ph]`.

[89] S. Catani and M. Grazzini, *Next-to-Next-to-Leading-Order Subtraction Formalism in Hadron Collisions and its Application to Higgs-boson Production at the Large Hadron Collider*, Phys. Rev. Lett. **98** (2007) 222002, arXiv: `hep-ph/0703012 [hep-ph]`.

[90] J. Alwall et al., *The automated computation of tree-level and next-to-leading order differential cross sections, and their matching to parton shower simulations*, JHEP **07** (2014) 079, arXiv: `1405.0301 [hep-ph]`.

[91] L. Lönnblad, *Correcting the Colour-Dipole Cascade Model with Fixed Order Matrix Elements*, JHEP **05** (2002) 046, arXiv: `hep-ph/0112284`.

[92] R. D. Ball et al., *Parton distributions for the LHC run II*, JHEP **04** (2015) 040, arXiv: `1410.8849 [hep-ph]`.

[93] P. Artoisenet, R. Frederix, O. Mattelaer and R. Rietkerk, *Automatic spin-entangled decays of heavy resonances in Monte Carlo simulations*, JHEP **03** (2013) 015, arXiv: `1212.3460 [hep-ph]`.

[94] H. B. Hartanto, B. Jäger, L. Reina and D. Wackeroth, *Higgs boson production in association with top quarks in the POWHEG BOX*, Phys. Rev. D **91** (2015) 094003, arXiv: `1501.04498 [hep-ph]`.

[95] S. Frixione, E. Laenen, P. Motylinski, C. White and B. R. Webber, *Single-top hadroproduction in association with a W boson*, JHEP **07** (2008) 029, arXiv: `0805.3067 [hep-ph]`.

[96] F. Demartin, B. Maier, F. Maltoni, K. Mawatari and M. Zaro, *tWH associated production at the LHC*, Eur. Phys. J. C **77** (2017) 34, arXiv: `1607.05862 [hep-ph]`.

[97] F. Demartin, F. Maltoni, K. Mawatari and M. Zaro, *Higgs production in association with a single top quark at the LHC*, Eur. Phys. J. C **75** (2015) 267, arXiv: `1504.00611 [hep-ph]`.

[98] D. J. Lange, *The EvtGen particle decay simulation package*, Nucl. Instrum. Meth. A **462** (2001) 152.

[99] ATLAS Collaboration, *ATLAS Pythia 8 tunes to 7 TeV data*, ATL-PHYS-PUB-2014-021, 2014, URL: `https://cds.cern.ch/record/1966419`.

[100] ATLAS Collaboration, *Object-based missing transverse momentum significance in the ATLAS Detector*, ATLAS-CONF-2018-038, 2018, URL: `https://cds.cern.ch/record/2630948`.

[101] M. Baak et al., *HistFitter software framework for statistical data analysis*, Eur. Phys. J. C **75** (2015) 153, arXiv: `1410.1280 [hep-ex]`.

[102] G. Cowan, K. Cranmer, E. Gross and O. Vitells, *Asymptotic formulae for likelihood-based tests of new physics*, Eur. Phys. J. C **71** (2011) 1554, arXiv: `1007.1727 [physics.data-an]`, Erratum: Eur. Phys. J. C **73** (2013) 2501.

[103] T. Junk, *Confidence level computation for combining searches with small statistics*, Nucl. Instrum. Meth. A **434** (1999) 435, arXiv: `hep-ex/9902006`.

[104] A. L. Read, *Presentation of search results: the CL_S technique*, J. Phys. G **28** (2002) 2693.

[105] C. G. Lester and D. J. Summers, *Measuring masses of semi-invisibly decaying particle pairs produced at hadron colliders*, Phys. Lett. B **463** (1999) 99, arXiv: `hep-ph/9906349`.

[106] A. Barr, C. Lester and P. Stephens, *m(T2): The Truth behind the glamour*, J. Phys. G **29** (2003) 2343, arXiv: `hep-ph/0304226`.

[107] ATLAS Collaboration, *Jet energy scale and resolution measured in proton–proton collisions at $\sqrt{s} = 13$ TeV with the ATLAS detector*, Eur. Phys. J. C **81** (2020) 689, arXiv: `2007.02645 [hep-ex]`.

[108] ATLAS Collaboration, *Formulae for Estimating Significance*, ATL-PHYS-PUB-2020-025, 2020, URL: `https://cds.cern.ch/record/2736148`.

[109] ATLAS Collaboration, *Search for top squark pair production in final states with one isolated lepton, jets, and missing transverse momentum in $\sqrt{s} = 8$ TeV pp collisions with the ATLAS detector*, JHEP **11** (2014) 118, arXiv: `1407.0583 [hep-ex]`.

[110] ATLAS Collaboration, *Search for top-squark pair production in final states with one lepton, jets, and missing transverse momentum using $36 fb^{-1}$ of $\sqrt{s} = 13$ TeV pp collision data with the ATLAS detector*, JHEP **06** (2018) 108, arXiv: `1711.11520 [hep-ex]`.

[111] M. L. Graesser and J. Shelton, *Hunting Mixed Top Squark Decays*, Phys. Rev. Lett. **111** (2013) 121802, arXiv: `1212.4495 [hep-ph]`.

[112] W. Verkerke and D. P. Kirkby, *The RooFit toolkit for data modeling*, eConf **C0303241** (2003) MOLT007, arXiv: `physics/0306116 [physics]`.

[113] L. Moneta et al., *The RooStats Project*, (2010), arXiv: `1009.1003 [physics.data-an]`.

[114] ATLAS Collaboration, *Constraints on new phenomena via Higgs boson couplings and invisible decays with the ATLAS detector*, JHEP **11** (2015) 206, arXiv: `1509.00672 [hep-ex]`.

[115] ATLAS Collaboration, *Measurement of Higgs boson decay into b-quarks in associated production with a top-quark pair in pp collisions at $\sqrt{s} = 13$ TeV with the ATLAS detector*, JHEP **06** (2021) 097, arXiv: `2111.06712 [hep-ex]`.

[116] ATLAS Collaboration, *Calibration of the ATLAS b-tagging algorithm in $t\bar{t}$ semileptonic events*, ATLAS-CONF-2018-045, 2018, URL: `https://cds.cern.ch/record/2638455`.

[117] ATLAS Collaboration, *Search for heavy particles decaying into top-quark pairs using lepton-plus-jets events in proton–proton collisions at $\sqrt{s} = 13$ TeV with the ATLAS detector*, Eur. Phys. J. C **78** (2018) 565, arXiv: `1804.10823 [hep-ex]`.